



CO₂ flux from the French Massif Central groundwaters: Modelling and quantitative estimation of the degassing process

Lisa Ricci, Francesco Frondini, Daniele Morgavi, Marino Vetuschi Zuccolini,
Guillaume Boudoire, Mickaël Laumonier, Stefano Caliro, Carlo Cardellini, Artur
Ionescu, Alessandra Ariano, et al.

► To cite this version:

Lisa Ricci, Francesco Frondini, Daniele Morgavi, Marino Vetuschi Zuccolini, Guillaume Boudoire, et al.. CO₂ flux from the French Massif Central groundwaters: Modelling and quantitative estimation of the degassing process. *Chemical Geology*, 2024, 652, <10.1016/j.chemgeo.2024.122012>. <hal-04753077>

HAL Id: hal-04753077

<https://hal.science/hal-04753077v1>

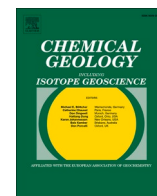
Submitted on 25 Oct 2024

HAL is a multi-disciplinary open access archive for the deposit and dissemination of scientific research documents, whether they are published or not. The documents may come from teaching and research institutions in France or abroad, or from public or private research centers.

L'archive ouverte pluridisciplinaire **HAL**, est destinée au dépôt et à la diffusion de documents scientifiques de niveau recherche, publiés ou non, émanant des établissements d'enseignement et de recherche français ou étrangers, des laboratoires publics ou privés.



Distributed under a Creative Commons CC BY-NC-ND 4.0 - Attribution - Non-commercial use - No
Derivative Works - International License



CO₂ flux from the French Massif Central groundwaters: Modelling and quantitative estimation of the degassing process

Lisa Ricci^{a,*}, Francesco Frondini^a, Daniele Morgavi^b, Marino Vetuschi Zuccolini^c,
Guillaume Boudoire^{d,e}, Mickael Laumonier^d, Stefano Caliro^f, Carlo Cardellini^{a,i},
Artur Ionescu^{a,g,h}, Alessandra Ariano^a, Giovanni Chiodiniⁱ

^a Dipartimento di Fisica e Geologia, Università di Perugia, via Pascoli snc, 06123 Perugia, Italy

^b Dipartimento di Scienze della Terra, dell'Ambiente e delle Risorse (DISTAR), Università degli Studi di Napoli Federico II, Via Vicinale Cupa Cinzia 21, 80126 Napoli, Italy

^c Dipartimento di Scienze della Terra, dell'Ambiente e della Vita (DISTAV), Università di Genova, Corso Europa 26, 16132 Genova, Italy

^d Laboratoire Magmas et Volcans, UCA, CNRD, IRD, OPGC, Campus universitaire des Cezeaux, 6 Av. Blaise Pascal, 63170 Aubière, France

^e Istituto Nazionale di Geofisica e Vulcanologia, Sezione di Palermo, Via Ugo la Malfa, 153, 90146 Palermo, Italy

^f Istituto Nazionale di Geofisica e Vulcanologia, Sezione di Napoli, Via Diocleziano, 328, 80125 Napoli, Italy

^g Universitatea Babeş-Bolyai, Department of Geology, Faculty of Biology and Geology, str. Mihail Kogalniceanu 1, Cluj-Napoca 400347, Romania

^h HUN-REN Institute for Nuclear Research (ATOMKI), Bem tér 18/c, 4026 Debrecen, Hungary

ⁱ Istituto Nazionale di Geofisica e Vulcanologia, Sezione di Bologna, Viale Carlo Berti Pichat, 6/2, 40127 Bologna, Italy

ARTICLE INFO

Editor: Christian France-Lanord

Keywords:

Earth degassing
CO₂ fluxes
Passive rifts
French Massif Central
Geochemical modelling

ABSTRACT

Passive rift systems are often characterized by CO₂ degassing, witnessed by the presence of mineral and thermal springs, bubbling pools, mofettes. Despite these field manifestations, the quantitative estimation of the CO₂ budget released to the atmosphere from these geodynamic structures is not well constrained. Here, we examine the chemistry of 169 springs, the isotopic composition of the dissolved carbon ($\delta^{13}\text{C}_{\text{TDIC}}$) of 33 springs and the dissolved gases composition of 6 springs from the French Massif Central, part of the European Cenozoic Rift System (ECRIS), in order to describe the CO₂ degassing process and to compute the CO₂ emission rate released from groundwaters at regional scale. Water-gas-rock models reveal that the separation of gas from the liquid phase occurs at P-T conditions between 10 bar–180 °C and 1 bar–10 °C. The carbon mass and isotopic balance of spring waters of the French Massif Central allow us to compute a total deeply-sourced CO₂ emission rate of $1.52 \pm 0.14 \times 10^9 \text{ mol yr}^{-1}$, suggesting that the CO₂ release from passive rift systems is significant at global scale and should be considered in the present-day global Earth degassing budget. The comparison of our data to other continental rift systems shows a high variability of CO₂ emission rates, highlighting that more detailed studies are needed to constrain the CO₂ flux from this geodynamic setting that, at present, is likely underestimated.

1. Introduction

Continental rifts, where the lithosphere is thinned by tectonic activity (Brune et al., 2023), are thought to be large CO₂ emitters (Kerrick, 2001) and could play an important role in the long-term carbon cycle and the related climate changes (Brune et al., 2017). However, due to the relatively low number of investigated areas (Brune et al., 2017), global estimates of the CO₂ emissions from these geodynamic settings are likely affected by large uncertainties. Some regional-scale estimations of the CO₂ emission have been completed in some active rifts, in particular in the East African Rift System (EAR; Lee et al., 2016; Hunt

et al., 2017), yet few data are available for passive rift structures. In addition, the different estimates of the total CO₂ emission for EAR demonstrate great uncertainty. In particular, Lee et al. (2016) computed a CO₂ emission rate of about $9 \times 10^{10} \text{ mol yr}^{-1}$ for the Magadi-Natron Basin (eastern branch of EAR) and, extrapolating this value, estimated a CO₂ emission rate of $0.9\text{--}2.4 \times 10^{12} \text{ mol yr}^{-1}$ for the entire EAR eastern branch. Meanwhile, Hunt et al. (2017) estimated a CO₂ emission rate of $1.2\text{--}9.9 \times 10^{10} \text{ mol yr}^{-1}$ from the central and northern sectors of the Main Ethiopian Rift (northernmost EAR system) and extrapolated an emission rate of $0.9\text{--}7.4 \times 10^{11} \text{ mol yr}^{-1}$ for the entire eastern branch of the EAR rift. These estimates range over one order of magnitude.

* Corresponding author.

E-mail address: lisa.ricci@studenti.unipg.it (L. Ricci).

<https://doi.org/10.1016/j.chemgeo.2024.122012>

Received 18 July 2023; Received in revised form 15 February 2024; Accepted 23 February 2024

Available online 24 February 2024

0009-2541/© 2024 The Authors. Published by Elsevier B.V. This is an open access article under the CC BY license (<http://creativecommons.org/licenses/by/4.0/>).

Quantitative estimations of CO₂ degassing are even more rare for passive rift systems and usually refer only to relatively small areas (e.g., the Escarot gas seep, Gal et al., 2018).

In this work, we focus on CO₂ degassing from the French Massif Central, which is located in central southern France and is part of the European Cenozoic Rift System (ECRIS, Fig. 1). ECRIS is a passive rift structure that crosses the central and western Europe for about 1100 km, from the Alpine foreland to the North Sea coast. The development of the ECRIS is related to the built-up of the Alpine and Pyrenean orogens (Dèzes et al., 2004), that induced lithospheric buckling, basin inversion, local intrusions of sodic magmas derived by variable degrees of mantle partial melting (Wilson and Downes, 2006), crustal thinning and numerous volcanic events in the European foreland. Even though the rifting stage of ECRIS ended in the Early Miocene (Michon and Merle, 2001), ECRIS is still affected by an ongoing degassing process, as evidenced by the presence of numerous bubbling pools, mofetes and CO₂-rich springs (Fouillac, 1983).

The chemical-isotopic composition of groundwaters (e.g. Pauwels et al., 1997) and of the free gas phase from bubbling mineral springs and mofetes of the French Massif Central (e.g.; Matthews et al., 1987; Bräuer et al., 2017) indicates a significant contribution of mantle-derived helium and carbon (Matthews et al., 1987; Battani et al., 2010; Bräuer et al., 2017). Nevertheless, the magnitude of the degassing process has rarely been quantified and only at a very small spatial scale. Aeschbach-Hertig et al. (1999) computed a mantle-related CO₂ emission rate of $1.7 \pm 0.6 \times 10^6 \text{ mol yr}^{-1}$ at Lac Pavin, a volcanic lake of 0.44 km²; Gal et al. (2018) estimated $1.8 \pm 0.4 \times 10^8 \text{ mol yr}^{-1}$ of deep seated CO₂ released through soil degassing from the 0.052 km² “Escarot” gas seep; Hermanson et al. (1991) computed a CO₂ flux of $7.82 \times 10^6 \text{ mol yr}^{-1} \text{ km}^{-2}$ through diffuse soil degassing from a not well specified granitic area of the French Massif Central.

The aim of this work is to investigate and quantify the deeply-derived CO₂ transported by the French Massif Central groundwaters, in an area which extends from Vichy to the north to Chaudes-Aigues to the south (Fig. 2). The area has been selected based on the high number and density of CO₂-rich springwaters.

In the following sections we consider the chemical and the isotopic composition of groundwaters and the chemical composition of dissolved

gases of the French Massif Central in order to propose different models that can explain the degassing process affecting the studied waters and to compute the deeply derived CO₂ emission rate on a regional scale.

2. Geological and hydrogeological setting of the study area

The French Massif Central (Fig. 1a) is the largest magmatic province of the western ECRIS (Michon and Merle, 2001; Fig. 1b) and consists of an uplifted plateau of Hercynian metamorphic and plutonic rocks (Downes et al., 2003), upon which Cenozoic volcanics are superimposed. The volcanic activity occurred from the Late Eocene to the Holocene, involving both fissure eruptions and central volcanoes (Downes et al., 2003). The study area (Fig. 2) is located in the central part of the French Massif Central and includes i) the western (main) sector of the French Massif Central volcanoes, from north to south: Chaîne des Puys, Monts Dore, Cézallier and Cantal, ii) the sedimentary Limagne Graben and iii) the metamorphic Combrailles region.

Monts Dore and Cantal are both central volcanoes. Cantal (2800 km², Reubi and Hernandez, 2000) is the largest and oldest stratovolcano of the Tertiary alkali province of France (Reubi and Hernandez, 2000) and was active between 11 and 2 Ma (Reubi and Hernandez, 2000). It gave rise to a wide range of magmatic compositions, from the oldest basanitic lavas, followed by trachyandesitic breccias (which represents the largest part of the volcanic edifice) to the youngest basaltic plateaus (Reubi and Hernandez, 2000). The younger Monts Dore massif (500 km², Nomade et al., 2014) is located northward the Cantal and was active between 3.1 Ma and 200 ka (Nomade et al., 2014). It consists of two volcanic edifices (the Guéry and the Sancy, Nomade et al., 2014) and the associated petrologic composition includes basaltic, tephritic, phonolitic, trachyandesitic and rhyolitic composition (Nomade et al., 2014). The Cézallier province is a basaltic plateau limited by the Monts Dore and the Cantal volcanoes. It formed between 8 and 3 Ma and consists in a stack of lava flows associated with scoria cones and phreatomagmatic deposits (Nehlig et al., 2003). Trachyphonolitic intrusions also occurred (Nehlig et al., 2003). The Chaîne des Puys extends northward the Monts Dore and consists of a 30 km-long volcanic chain with a N-S orientation, constituted by about 80 aligned monogenetic cones associated to alkaline intraplate magmatism (Maury et al., 1980; Merle et al., 2023).

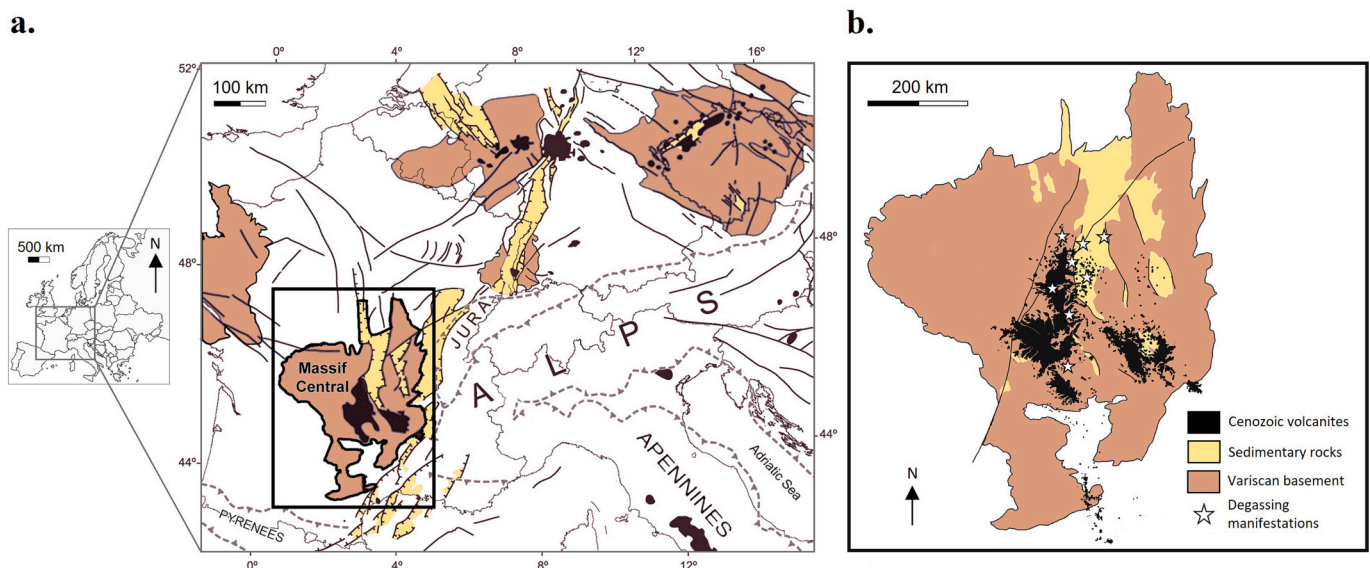


Fig. 1. a. Location of the French Massif Central in the European Cenozoic Rift System. Solid barbed line outlines the Variscan deformation front; stippled barbed lines symbolize the Alpine deformation front (after Dèzes et al., 2004). b. Simplified geological map of the French Massif Central (modified after Michon and Merle, 2001; Nehlig et al., 2003). Main degassing areas are highlighted through white stars. Figures also show main fault systems (black line), rift-related sedimentary basins (yellow), Variscan massifs (brown) and volcanic fields (black). (For interpretation of the references to colour in this figure legend, the reader is referred to the web version of this article.)

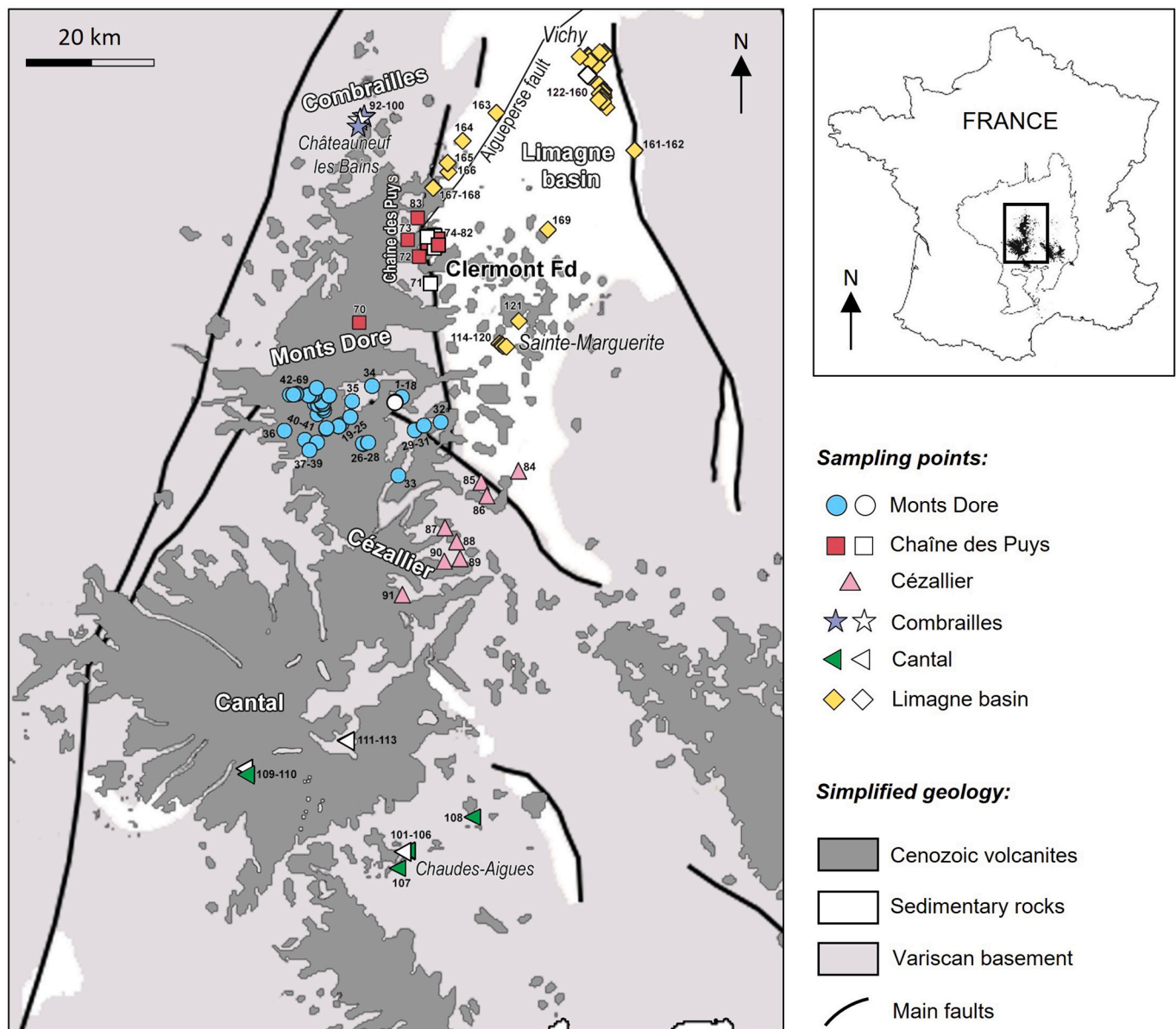


Fig. 2. Location of the sampling points and simplified geological and structural setting of the study area. The shape of the symbol identifies each group; full colour symbols are springs; white symbols are wells. Geological and structural setting is modified after Michon and Merle (2001) and Nehlig et al. (2003).

The hydrological setting of these volcanic areas is characterized by shallow aquifers hosted in the alkaline volcanics that overlie a lower aquifer hosted in the Variscan basement, mainly made by orthogneiss, paragneiss and granites. The water circulation is driven by NE-SW or N-S fault systems inherited from the Hercynian period (and reactivated during the rifting stage, Michon and Merle, 2001) or by fractures resulting from the caldera. In the Cantal and Monts Dore provinces, meteoric waters infiltrate at 1400–1600 m a.s.l. and circulate first through the volcanics, then in the underlying basement (Bérard et al., 2002a, 2002b). Where they emerge, groundwaters are both thermal and cold, reaching a maximum temperature of 82 °C (Source du Par, Chaudes-Aigues). In the Monts Dore, structural control is given by the so-called Haute-Dordogne caldera fault (Pauwels et al., 1997), along which mineral springs of the Dordogne Valley issue. In the Cantal, the water follows the main and secondary drainages, given by rock foliations, fissures, fractures and secondary horizons with distinct permeability (e.g., low-permeable quartz and microgranites veins, which cut the gneissic and schistose Cantal basement and control the hydrology, Bérard et al., 2002b). At Cézaillier, mineral springs emerge from the

deeply fractured Variscan basement (Casanova et al., 1999), here made of ortho- and paragneiss, amphibolites and migmatites (Nègre et al., 2000). In the Chaîne des Puys, water flows down through the volcanic edifices and lava flows due to their high permeability and accumulates at the interface between the volcanics and the less permeable crystalline basement, which act as a substratum (Aumar, 2022). The water circulation is strongly dictated by the orientation of paleo valleys and Variscan faults (Merle et al., 2023). The Chaîne des Puys lava flow deposits define two main aquifers: the northern system, where water flows with a NE-SW direction; the southern aquifer, where the circulation occurs with a NW-SE direction (Merle et al., 2023). The Limagne basin is the main semi-graben of the French Massif Central. It extends in the northern part of the region and exhibits a N-S orientation. This rift-related basin is permeated by large scale normal faults that caused the envelopment of sub-basins within the main graben and drives fluid circulation. Here, mineral springs occur along the Allier valley, at Vichy basin and Sainte-Marguerite, and along the Aigueperse fault. The majority of the Limagne basin waters are thermal and clearly show a high CO₂ content (Michard et al., 1976), demonstrated by the presence of

bubbles where the springs issue. For Vichy basin, Michard et al., 1976 suggest a water circulation through the granitic basement, where thermal features are acquired and a consequent rise through faults and fractures cutting both the basement and the sedimentary cover. The sedimentary deposits at Vichy basin can also act as shallow aquifers (Michard et al., 1976). Both at Sainte-Marguerite and along the Aigueperse fault the circulation is controlled by the fault system and water circulates through the granites of the basement but also interact with the sedimentary cover (Battani et al., 2010; Millot et al., 2007). In the metamorphic Combrailles region, mineral springs occur at Châteauneuf-Bains. These thermal waters, of meteoric origin, directly emerge from the granitic, highly fractured basement, where they acquire the mineralization (Bertin et al., 2003).

3. Materials and methods

3.1. Groundwater sampling and analysis

Groundwater from 29 springs (Supplementary material 1) were collected in 2006, 2009, 2010 and 2021. Temperature, pH, Eh and electrical conductivity were measured directly in the field by using WTW pH-Eh/cond 3320 multi-meter. The HCO_3^- content was measured in the field, through acid titration with HCl 0.01 N, using methyl orange as indicator (error = 1%). Dissolved silica was determined by standard colorimetric method in the field. Water samples for chemical and isotopic (δD , $\delta^{18}\text{O}$) analyses were collected in 100 mL polyethylene bottles. The water aliquot for anion determination was filtered through 0.45 μm membrane filters while the water aliquots for cations were filtered and immediately acidified with 1% of 1:1 diluted HCl . Water samples for the determination of isotopic composition of total dissolved inorganic carbon ($\delta^{13}\text{C}_{\text{TDIC}}$) were collected in 1000 or 500 mL polyethylene bottles, depending on the expected bicarbonate content. The dissolved carbon was precipitated directly on field as SrCO_3 , by adding SrCl_2 and NaOH to the water sample. The precipitated carbonates were filtered, washed with distilled water and dried in an N_2 atmosphere. Dissolved gases (CO_2 , N_2 , O_2 , Ar, He) were sampled on 6 springs (samples 26, 30, 70, 72, 114, 121) using pre-evacuated 250 mL glass vials equipped with a three-way glass valve or a Thorion valve, filling the sampler up to 65–80% (V_{liq}) of its volume (V_{tot}), following the methodology described by Chiodini (1996) and Caliro et al. (2005).

Major dissolved ions were determined at the geochemical laboratory of the Department of Physics and Geology of Perugia University. Ca and Mg concentrations were determined by atomic absorption (AA) flame spectroscopy while Na, K and Li were determined by atomic emission (AE) flame spectroscopy, using an IL 951 AA/AE spectrometer. Cl, SO_4 , NO_3 and F were determined by ion chromatography, using a Dionex DX-120 Ion Chromatograph. Carbon, oxygen and hydrogen isotopes analyses were performed by means of standard mass spectrometry techniques at the Geochemistry Laboratory of the Istituto Nazionale di Geofisica e Vulcanologia-Osservatorio Vesuviano (INGV-OV) Napoli, using a Finnigan Delta plusXP continuous flow mass spectrometer (MS) coupled with a GasbenchII device (GBII) (analytical errors: $\delta\text{D} \pm 1\text{‰}$, $\delta^{18}\text{O} \pm 0.08\text{‰}$ and $\delta^{13}\text{C} \pm 0.06\text{‰}$). Isotopic compositions are given in ‰ notation per mill versus V-PDB for carbon and versus V-SMOW for oxygen and hydrogen. The dissolved gas phase, separated in the head-space of the vial ($V_{\text{gas}} = V_{\text{tot}} - V_{\text{liq}}$), was analyzed by a gas chromatograph equipped with a Thermal Conductivity (TCD) detector, according to Chiodini (1996) and Caliro et al. (2005), using He as carrier gas. The partial pressure of each gas species (CO_2 , N_2 , O_2 , Ar and CH_4) was determined with reference to standards at different pressures. Helium partial pressures were determined in the same injection by a leak detector (detection limit 0.00015 mbar).

3.2. The geochemical database

The data collected in this study (29 springs, Supplementary material

1) were integrated with bibliographic data, producing a dataset (Supplementary material 1) containing the chemical analysis of 169 samples (149 springs and 20 wells), the water isotopic composition of 85 samples, the carbon isotopic composition of 33 samples and the dissolved gas composition of 6 samples. The analytical error, evaluated checking the charge balance, is lower than 2% for 59% of the samples and is about 3.2% on average. The flow rates of all sampled springs (Supplementary material 1) were measured on site measuring the time necessary to fill a 50 L container (error 10%), with the exception of Grand Barbier 2 (sample 58) and Volvic (sample 83), which are bottled for drinking, and five springs from Vichy (sample 122, 125–127, 131), that are used for both spa and drinking. The flow rate of Grand Barbier 2 was estimated from production data (Bérard et al., 2002a) and the flow rate of Volvic and Vichy springs are measured and publicly displayed by the management companies on tables placed at the entrance to the spas/bottling plant. Finally, for literature data we considered the flow rate reported in the original works (Supplementary material 1).

3.3. Aqueous speciation and geochemical modelling

The speciation of the solutions, the total dissolved inorganic carbon (TDIC), the partial pressure of carbon dioxide ($p\text{CO}_2$), and saturation indexes of the studied water were computed through the PHREEQC version 3 code (Parkhurst and Appelo, 2013), using the *lnl.dat* thermodynamic database (Delany and Lundeen, 1990; Wolery, 1979; Wolery, 1992; Wolery and Jarek, 2003).

The PHREEQC version 3 code has been used also to compute three theoretical models describing the evolution of an infiltrating water that interacts with a deep gas phase and with the host rocks, following the methodology described by Caliro et al. (2005).

4. Results and discussions

4.1. Chemical composition of waters

Springs and wells are characterized by temperatures ranging between 4.2 and 82 °C and total dissolved solids (TDS) between 24 and 9694 mg L^{-1} , with almost half of samples (44%) showing TDS higher than 5000 mg L^{-1} . The majority of springs exhibit low flow rates ($\sim 1 \text{ L s}^{-1}$ on average). The total water flow discharged from the sampled springs is about 0.58 $\text{m}^3 \text{ s}^{-1}$, which is a significant fraction of the total water circulating in the French Massif Central aquifers (e.g. the amount of water circulating in the volcanic aquifers is estimated to be 1.27 $\text{m}^3 \text{ s}^{-1}$ by Maréchal and Rouillard, 2020). Almost all the analyzed waters are acidic, with pH ranging from 3.39 to 7.85 (average pH ~ 6.4). The most acidic waters are “La Sulfureuse” and Lavina Edembouche springs, both located on the Puy de Sancy (Monts Dore) at about 1600 m a.s.l., characterized by a pH of 4.00 and 3.39 respectively.

The Langelier-Ludwig diagram (Fig. 3a) and the $\text{SO}_4\text{-Cl-HCO}_3$ diagram (Fig. 3b) show that the majority of the investigated waters (66%) are bicarbonate-alkaline waters, 26% are bicarbonate-earth alkaline waters and only 8% show a chloride-alkaline or Earth-alkaline composition. The high HCO_3^- content of the majority of samples suggests that the main water-rock interaction processes (e.g. volcanic glass dissolution and incongruent dissolution of silicate minerals) are related to the first dissociation of the carbonic acid. Fig. 3a also highlights that the French Massif Central waters are characterized by an high chemical variability due to several processes, such as i) mixing between a deep mineralized component and freshwater, as in the case of Monts Dore waters (Pauwels et al., 1997) and Cézaillier springs (Vuataz et al., 1987; Nègre et al., 2000); ii) circulation in different lithotypes (metamorphic basement, volcanics and sedimentary formations), as described in section 2. and iii) distinct degree of the water-rock interaction (Millot et al., 2007).

Most of the bicarbonate-alkaline waters (i.e. Cézaillier, Combrailles, Saint-Nectaire) circulate in the metamorphic basement. Vichy waters,

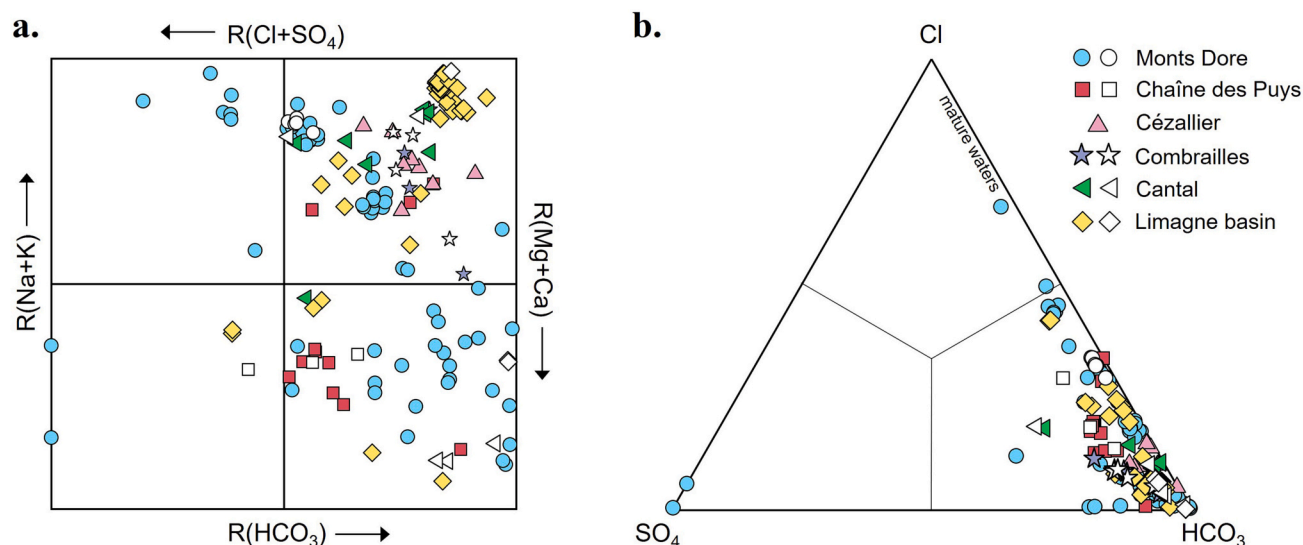


Fig. 3. a. Langelier-Ludwig diagram. b. Cl-SO₄-HCO₃ ternary diagram (Giggenbach and Goguel, 1989).

that constitute a cluster close to the top-right vertex of Fig. 3a, represent a much more complex case. In fact, as described by Michard et al., 1976, these waters equilibrate with quartz and K-feldspar in the granitic basement, where they acquire part of their mineralization and are then enriched in a CO₂-rich phase (Michard et al., 1976). During the rise toward the surface, they circulate in the sedimentary rocks of the Limagne basin, composed by conglomerates and sandstones, marls and/or limestones and evaporitic deposits (Vennin et al., 2021), where they acquire their definitive fingerprint, through the partial dissolution of the host-rock minerals (i.e. leaching of Ca, Sr, Mg from carbonate minerals and K and remobilization of silica and aluminium, Michard et al., 1976).

Bicarbonate-earth alkaline waters are characterized by lower TDS values. Generally, these waters are characterized by a rapid circulation in shallow, volcanic and sedimentary aquifers or they result in the mixing of deep mineralized fluids with freshwaters, as in the case of Monts Dore (Pauwels et al., 1997) and Cézaillier springs (Vuataz et al., 1987; Nègre et al., 2000).

All the chloride-alkaline springs are located along the Dordogne valley and their high chloride and sodium contents is probably related to long residence times (“mature waters” in Fig. 3b, according to (Pauwels et al., 1997). “La Sulfureuse” and “Lavina Edembouche” springs show a sulfate-acid composition. Their relatively low Ca content, 5.3 mg L⁻¹ and 18.0 mg L⁻¹ respectively, and their salinity, 96 mg L⁻¹ and 292 mg L⁻¹ respectively, excludes the dissolution of gypsum as the major source of sulfate, while the low pH suggests that the oxidation of H₂S or S-bearing minerals (i.e. pyrite and chalcopyrite) are the processes causing both the SO₄ increase and the decrease the pH to values of about 4 or lower. According to Pauwels et al. (1997) the S-bearing minerals occurring in concomitance of ancient fumarole deposits, play a role in providing sulphate into Monts Dore waters.

4.2. Geothermometry

Na/K geothermometers (Fournier, 1979) show temperatures from 177 to 347 (Table 1), in agreement with those computed by Serra et al. (2003), while the temperature estimations performed using the empirical Na–Li geothermometer (Michard, 1990), range from about 100 to about 260 °C (Table 1). Different areas have different temperatures. In the Monts Dore area, the Na/K temperatures are in an interval between 241 and 347 °C, while the Na/Li temperatures range from 100 to 237 °C. Within this group, Na/K temperatures are significantly higher than Na/Li temperatures for most of the springs, except for Saint-Nectaire, where the two temperature estimates are very similar. At Cézaillier and Cantal

Table 1

Reservoir temperatures, computed with the Na/K geothermometer (Fournier, 1979) and Na/Li geothermometer (Michard, 1990).

Group	Sub-group	T _{Na/K} (°C)	T _{Na/Li} (°C)
		Fournier (1979)	Michard (1990)
Monts Dore	Saint-Nectaire	241	237
	Le Mont-Dore, La Bourboule,	259	170
	Couze Pavin valley		
Cézaillier	Chaudes-Aigues	347	100
	Cézaillier	238	202
Cantal	Chaudes-Aigues	221	171
Combrailles	Châteauneuf-les-Bains	185	266
Limagne Basin	Sainte-Marguerite	238	186
	Vichy	177	149
	Aigueperse fault	235	214

the temperatures computed with the Na/K geothermometer (238, 221 °C) are higher than the Na/Li temperatures (202, 171 °C) while at Châteauneuf-les-Bains Na/K temperatures (185 °C) are lower than the Na/Li estimates (266 °C). Finally, in the Limagne Basin it has been computed a temperature interval between 149 and 214 °C with the Na/Li geothermometer and from 177 °C to 238 °C with the Na/K geothermometers.

It should be noted that, according to the Na-K-Mg ternary diagram proposed by Giggenbach (1988), (Fig. 4), about 78% of the samples represents immature waters, far from the equilibrium with a stable silicate mineral assemblage, 22% are partially equilibrated with silicates, meaning that equilibrium is attained with respect to plagioclase and K-feldspar, but not with respect to Mg-bearing silicates, and no samples fall along the full equilibrium curve.

According to Giggenbach (1988), only samples falling in the full and/or partial equilibrium fields can be used for the estimation based on Na/K geothermometers. Considering that only 22% of our samples are in equilibrium with plagioclase and K-feldspar, the temperature estimations based on the Na/Li geothermometer are probably more reliable than the estimation based on the Na/K ratio.

The Na/Li temperatures are in good agreement with the temperatures reported by Serra et al. (2003) and show that the highest temperatures, generally higher than 200 °C, are attained at Saint-Nectaire, in the Monts Dore area, at Châteauneuf-les-Bains, in the Combrailles region and along the Aigueperse fault. All the other systems are characterized reservoir temperature between 100 and about 180 °C.

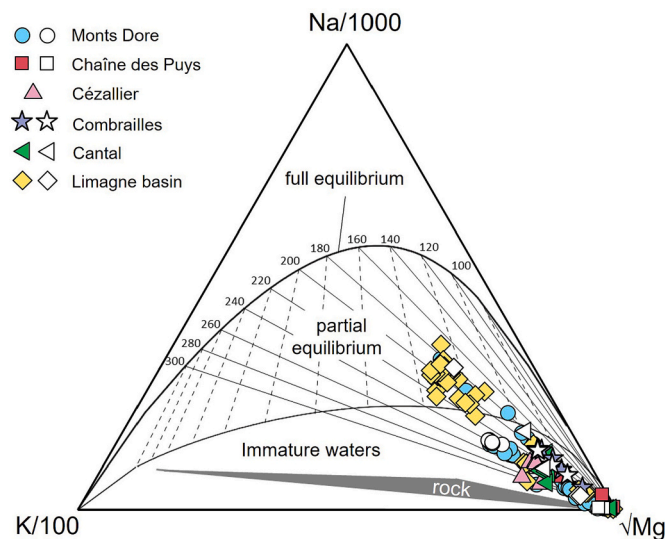


Fig. 4. Na-K-Mg ternary diagram (modified from Giggenbach, 1988).

4.3. Stable isotopes of water

Figs. 5a and 5b show the δD and $\delta^{18}O$ values of sampled waters: δD ranges from -65.9‰ to -55.5‰ and $\delta^{18}O$ varies between -10.20‰ and -8.10‰ . Most of the samples fall between the global meteoric water line (GMWL; Craig, 1961) and the regional meteoric water line (RMWL; Fouillac et al., 1991), suggesting a prevailing meteoric origin of thermal waters. These waters are characterized by values of deuterium excess ($d = \delta D - 8\delta^{18}O$) from 8.60‰ to 21.70‰ (12.36‰ on average), in the range of predicted evaporation d in the Atlantic Ocean at mid latitudes (Pfahl and Soderemann, 2014). Lower d values characterize the waters of La Gargouillère and Grand Saladis springs (7.17‰ and -10.21‰ respectively) and three drill holes at Saint-Nectaire (d values between 3.96‰ and 7.22‰). The first two springs, located in the Sainte-Marguerite area, plot to the right of both meteoric water lines and their isotopic composition could be explained by the evaporation of groundwater after the discharge at surface. Field evidence, like the presence of

evaporative ponds around the main discharge, support this hypothesis. The regression line computed from the values of Grand Saladis and La Gargouillère, along with the other unevaporated springs of the area, is:

$$\delta D = 4.87 \times \delta^{18}O - 17.63 \quad (1)$$

The Eq. (1) closely fits the data ($R^2 = 0.98$; standard error of the estimate $SE = \pm 1.92\text{‰}$). Its slope (4.87) is consistent with slopes predicted on the basis of a steady state evaporation model of surface waters at mid latitudes (Gibson et al., 2008), ranging from three to five. Taking into account the slope deviation from the GMWL and the low deuterium excess, the regression can be interpreted as a local evaporation line of spring waters after discharge in the Sainte-Marguerite area (LEL in Fig. 5). Also, waters from the three drill holes of Saint-Nectaire plot to the right of both meteoric water lines, showing a depletion in ^{18}O without variations in the δD . This signature may be interpreted with an oxygen exchange with the silicate of the hosting rocks, as suggested by Pauwels et al., 1997. Some samples from the Cézallier and Mont-Dore regions show a slight shift to the left of both meteoric water lines. This horizontal shift, consistent with the literature data (Pauwels et al., 1997; Casanova et al., 1999) is typical of CO_2 -rich groundwater and is likely related to oxygen exchange between CO_2 and water, according to the following reaction (D'Amore and Panichi, 1985; Karolytė et al., 2017):



Considering that waters discharged by the springs in the area are of meteoric origin, their ^{18}O content reflects the original composition of rainwater, that essentially derives from the combination of two effects: i) the *continental effect*, which is the gradual depletion of the residual marine moisture in heavy isotopes during the air masses movement from the coast to inland and ii) the *altitude effect*, consisting in the stepwise depletion in ^{18}O (and D) isotopes increasing the elevation. A recent estimation of the continental effect in French territory is given by Millot et al. (2010), that computed a value of -3.2‰ $\delta^{18}O/1000$ km moving inland from the Atlantic coast. Furthermore, Ladouche et al., 2009 assumed a vertical isotopic gradient of $-2.7\text{‰}/\text{km}$ in the area of Montpellier (about 200 km south of Clermont-Ferrand), in good agreement with the global average elevation gradient ($-2.8\text{‰}/\text{km}$, Kern et al., 2020) and with the local European one as in Poage and

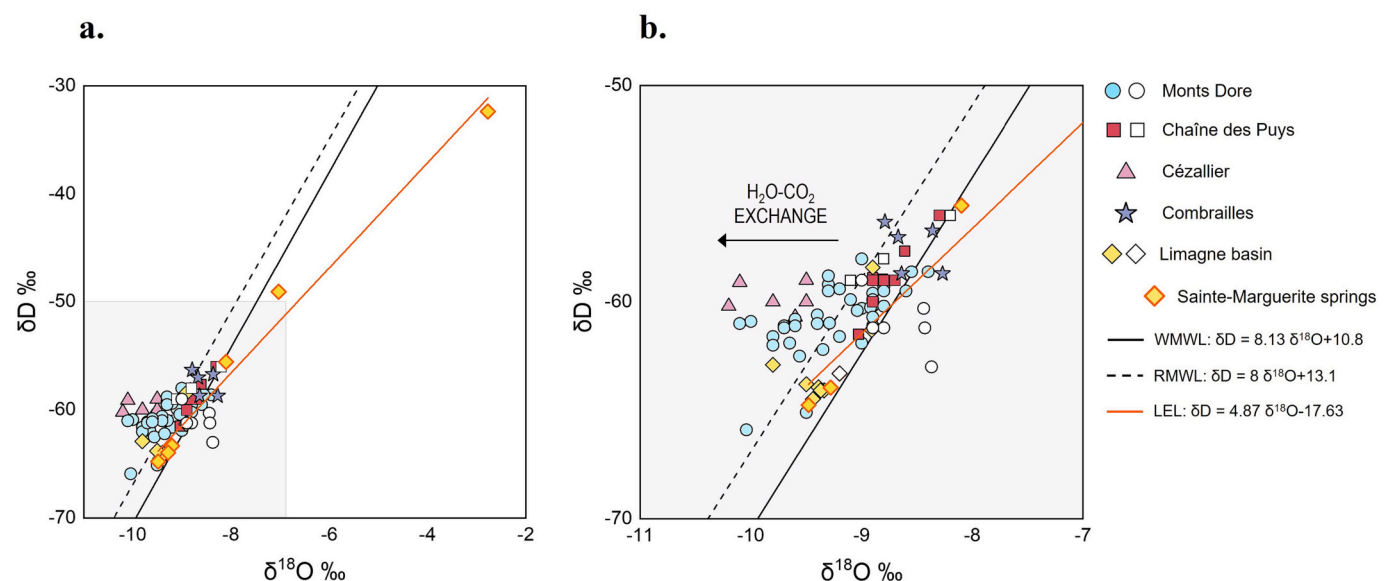


Fig. 5. a. δD vs $\delta^{18}O$ diagram. The orange line is the local evaporation line (LEL) related to the Sainte-Marguerite samples. Solid line is the World Meteoric Water Line (WMWL, Craig, 1961); dashed line is the Regional Meteoric Water Line (RMWL, Fouillac et al., 1991). b. Detail of Fig. 5a in the range indicated by the grey rectangle. Black arrow highlights the process of isotopic exchange between water and carbon dioxide oxygen. (For interpretation of the references to color in this figure legend, the reader is referred to the web version of this article.)

Chamberlain (2001). The altitudes of the recharge area, computed by correcting the $\delta^{18}\text{O}$ value for the $\text{CO}_2\text{-H}_2\text{O}$ exchange and excluding the samples affected by evaporation, range between 800 and 1300 m.

4.4. Dissolved gases

During July 2021, six samples were collected from Monts Dore, Chaîne des Puys and Limagne basin for the determination of the chemical composition of the dissolved gasses. The content of non-reactive gaseous species He, Ar and N_2 is shown in the ternary diagram of Fig. 6a.

Here, as reference, are reported the compositions of air and air saturated water (ASW), computed with the PHREEQC version 3 code equilibrating the average meteoric water collected near Sainte-Marguerite (Nègre and Roy, 1998) with the atmospheric gases.

Fig. 6a highlights that the analyzed samples are not contaminated with air and plot along a mixing line between the ASW and a helium-rich gas phase, of probable deep origin. This is also suggested by Fontaine Goyon (sample 26), plotting near the He vertex, characterized by $R/\text{Ra} = 4.74$ and $R/\text{Ra} = 5.69$ after correction for atmospheric helium (Bräuer

et al., 2017).

In order to interpret the dissolved gas data, the chemical compositions have been compared to three theoretical models describing the evolution of an infiltrating water that interacts with the host rocks and with a deep gas phase (Figs. 6b and c). Model 1, no sink model (Chiodini et al., 2000) is obtained adding to ASW 0.28 mol kg^{-1} of deep gas (DG) in 280 steps, assuming that no CO_2 degassing and no calcite precipitation occur during the addition of the deep gas phase. In this model the confining pressure is always higher than gas pressure. Model 2 is obtained assuming continuous degassing at 1 bar and 10°C (corresponding to aquifer-atmosphere interface) during the addition in 1000 steps of 1 mol kg^{-1} of DG and $0.061 \text{ mol kg}^{-1}$ of volcanic glass. Model 3 is obtained assuming continuous degassing at 10 bar and 180°C during the addition of 1 mol kg^{-1} of DG and $0.061 \text{ mol kg}^{-1}$ of volcanic glass, in 1000 steps. The pressure used in Model 3 is the maximum $p\text{CO}_2$ at which the studied samples equilibrate with calcite (assuming that systems oversaturated with calcite at surface were in equilibrium with this mineral prior to the CO_2 degassing), corresponding approximately to a 100 m water column. The temperature of Model 3 is the average T computed with the Na/Li geothermometers.

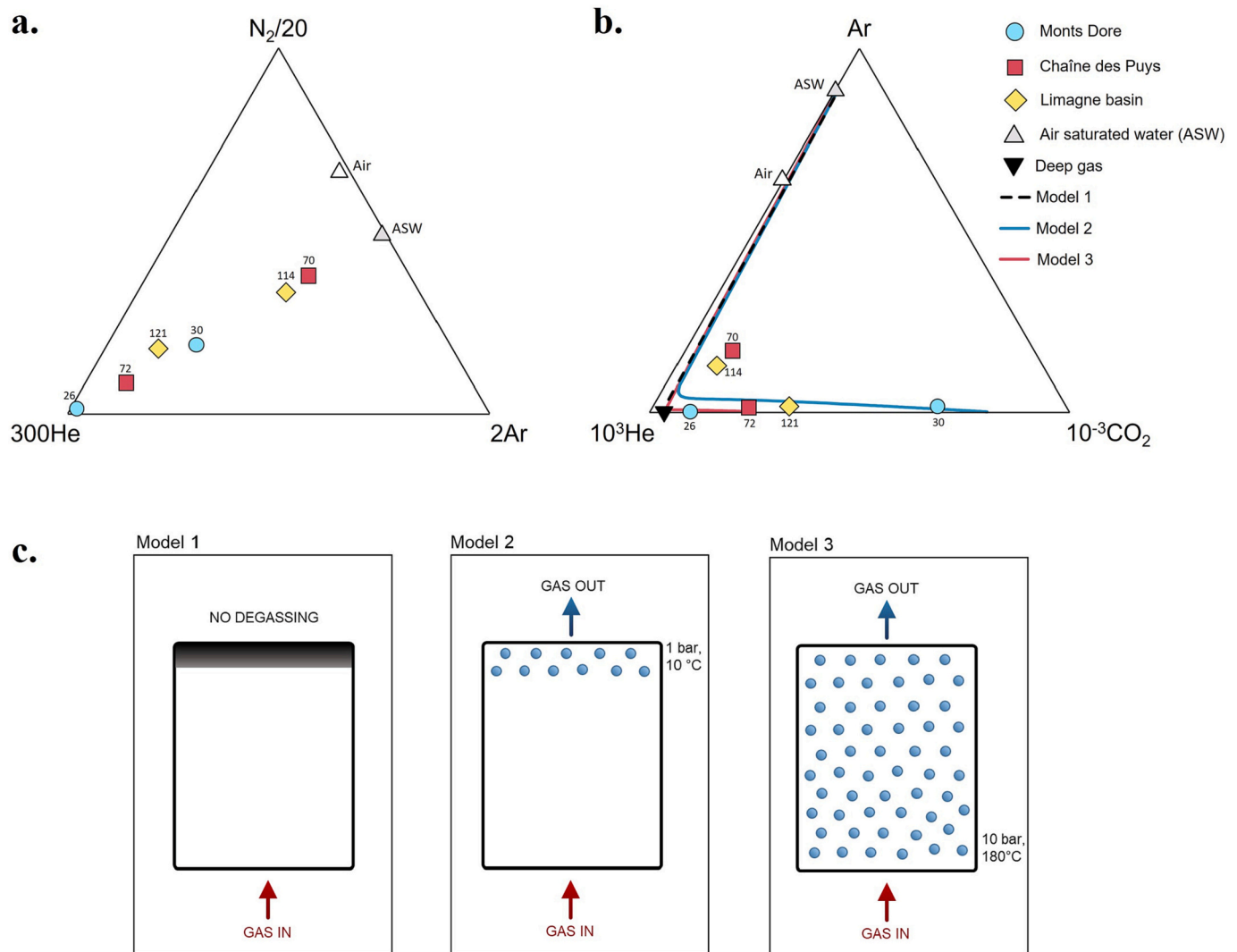


Fig. 6. a. Ternary diagram of relative abundances of Ar- N_2 -He of the studied samples, showing also the composition of air saturated water (ASW, grey triangle) and air (open triangle). b. Ternary diagram of relative abundances of He-Ar- CO_2 , showing the composition of ASW, air, deep gas and the evolution trends predicted by Model 1 (dashed black line), Model 2 (blue line) and Model 3 (red line). c. Conceptual models illustrating the three theoretical models: in Model 1 the confining pressure is always higher than the gas pressure; in Model 2 the gas phase separation with bubbles formation occurs just below the water table; in Model 3 the gas separation occurs at 10 bar, corresponding approximately to a 100 m water column. (For interpretation of the references to colour in this figure legend, the reader is referred to the web version of this article.)

The methodology used to compute Model 2 and Model 3 is described in detail in Caliro et al. (2005). The dissolved rock has been defined as a volcanic glass with the average chemical composition of the French Massif Central volcanic rocks, downloaded from the GEOROC database (on 10 February 2023, Lehnert et al., 2000). The rock composition used in the models is the one that better represents the average infiltration areas of the study area, however other models have been computed considering the same P/T conditions but other rock compositions and a detailed discussion about the influence of rock composition on CO₂ degassing is given in the Supplementary material 2.

The amount of dissolved rock (0.061 mol kg⁻¹) has been evaluated as the average amount of cations related to glass dissolution, computed for each sample by subtracting the equivalents of Cl, NO₃ and SO₄ from the sum of Ca, Mg, Na and K as described in Caliro et al. (2005).

The deep gas (DG) phase has been defined as a mixture of CO₂, He, Ar and N₂ and its composition (Table 2) is that of the free gas phase released in the Monts Dore area from the Escarot mofette, which best represents the volatiles derived from the Subcontinental lithospheric mantle (SCLM) beneath ECRIS (Bräuer et al., 2017).

In Models 2 and 3, during the incremental addition of the DG, the solution progressively degasses and, when the oversaturation in calcite is achieved, the precipitation of this mineral phase begins. At each step the content of dissolved species, the amount of each gas species exsolved from the solution and the amount of precipitated calcite have been computed.

The theoretical models are compared to the dissolved gas data in Fig. 6b. Model 1, represented by a straight line joining the ASW to the DG, does not explain the composition of our samples (dashed line in Fig. 6b). Model 2 (blue curve in Fig. 6b) and Model 3 (red curve in Fig. 6b) show a similar trend. The addition of the DG phase in the first steps moves the composition of dissolved gasses toward He vertex. Helium and argon are released (i.e. degassed) before CO₂ because of their lower solubility in water. Further addition of the DG moves the composition computed by both models toward the CO₂ vertex. Model 2 better explains the composition of samples 30 and 121, while Model 3 interpolates with a good accuracy samples 26 and 72. Samples 70 and 114, the closest to the ASW in Fig. 6a., can be interpreted as groundwaters that have been remixed with surficial waters.

4.5. Evolution of C_{ext} and δ¹³C_{ext}

The “external carbon” (C_{ext}) and δ¹³C of external carbon (δ¹³C_{ext}) of the French Massif Central waters are reported in Fig. 7. C_{ext} represents the fraction of TDIC deriving from sources external to the aquifer (i.e. atmospheric, biogenic and deeply produced CO₂), thus excluding the contribution coming from carbonate mineral dissolution (C_{carb}, Chiodini et al., 2000; Chiodini et al., 2004; Frondini et al., 2019) and is computed by the equations:

$$C_{\text{ext}} = \text{TDIC} - C_{\text{carb}} \quad (3)$$

and,

$$C_{\text{carb}} = m\text{Ca} + m\text{Mg} - m\text{SO}_4 \quad (4)$$

where mCa, mMg and mSO₄ are the concentration of dissolved Ca, Mg and SO₄ respectively.

Most samples are located in volcanic areas, as in the case of Monts Dore and Cézallier springs, or directly emerge from the granitic

Table 2

Chemical and isotopic composition of the deep gas (DG) used in the theoretical models (after Bräuer et al., 2017).

CO ₂	Ar	He	N ₂	δ ¹³ C
%	%	%	%	‰
99.34	5.81 × 10 ⁻³	2.83 × 10 ⁻³	6.51 × 10 ⁻¹	-3.6

basement through fault systems (as Sainte-Marguerite and Combrailles springs). This means that the contribution of C_{carb} can be assumed as negligible, resulting in C_{ext} = TDIC; δ¹³C_{ext} = δ¹³C_{TDIC}. In the case of Vichy basin springs (samples 122–160), Aigueperse fault springs (samples 163–169) and Châteldon waters (samples 161–162), the correction for the C_{carb} has been applied. The δ¹³C_{ext} of these samples has been computed according to Frondini et al. (2019), using a δ¹³C_{carb} = 1.4‰, resulting by the average of Eocene-Oligocene carbonates of Mediterranean (Bodiselsch et al., 2004; Cornacchia et al., 2018).

In order to interpret the carbon isotopic composition, C_{ext} and δ¹³C_{ext} of the sampled waters are compared to the three theoretical models, Model 1, Model 2 and Model 3, described in the previous section (Fig. 7). For each model, the values of C_{ext} and δ¹³C_{ext} were computed from:

$$C_{\text{ext},x} = C_{\text{ext},(x-1)} - \Delta\text{calcite} - \Delta\text{CO}_2 + C_{\text{deep}} \quad (5)$$

$$\delta^{13}\text{C}_{\text{ext},x} = \left[C_{\text{ext},(x-1)} \times \delta^{13}\text{C}_{\text{ext},(x-1)} - (\Delta\text{calcite} \times \delta^{13}\text{C}_{\text{calcite}}) - (\Delta\text{CO}_2 \times \delta^{13}\text{C}_{\text{CO}_2}) + C_{\text{deep}} \times \delta^{13}\text{C}_{\text{deep}} \right] / C_{\text{ext},x} \quad (6)$$

where C_{ext} is computed with the PHREEQC version 3 code, C_{deep} is the DG added to the solution, Δcalcite and ΔCO₂ represent the amounts of precipitated calcite and of degassed CO₂ (the amount of CO₂ that exsolves from the solution, forming bubbles) computed at each step. In the No-sink Model, Δcalcite and ΔCO₂ are set to zero.

In all the three models (i) the carbon isotopic composition of the DG (δ¹³C_{deep}) is assumed to be -3.6‰ (corresponding to δ¹³C_{CO₂} of Escarot mofette and in agreement with the range of variation of the SCLM beneath ECRIS, according to Bräuer et al., 2017 and Boudoire et al., 2023) (ii) δ¹³C_{calcite} and δ¹³C_{CO₂} are computed considering the fractionation factors for the carbonate system (Clark and Fritz, 1997) and (iii) the C_{ext} and the δ¹³C_{ext} of Grand Barbier 2 spring (sample 58; 4.91 × 10⁻⁴ mol kg⁻¹ and -16.78‰, respectively) are assumed to be representative of the infiltrating water because of the low C_{ext} and its low ¹³C content, both suggesting the absence of any C_{deep} inputs (Chiodini et al., 2000).

In Model 1, the addition of the DG phase causes an increase in the δ¹³C_{ext} following a hyperbolic trend, asymptotic to the δ¹³C_{deep} value. Model 2 follows the trend of Model 1 up to C_{ext} = 1.10 × 10⁻² mol kg⁻¹ and δ¹³C_{TDIC} = -4.09‰, then shifts upward, reaching δ¹³C_{ext} of +4.19‰ at the end of the simulation (corresponding to C_{ext} = 1.43 × 10⁻¹ mol kg⁻¹). This is due to the progressive degassing of CO₂ (separation of a free gas phase), occurring from C_{ext} of 7.88 × 10⁻³ mol kg⁻¹ and the precipitation of calcite, starting at C_{ext} = 1.16 × 10⁻¹ mol kg⁻¹. Model 3 shows the same trend of Model 2, but the deviation from Model 1 occurs at higher C_{ext} content (C_{ext} = 8.07 × 10⁻² mol kg⁻¹; δ¹³C_{ext} = -3.68‰). This is explained by the higher total gas pressure (10 bar), that hampers the degassing process and the consequent carbonates precipitation. Therefore, the three models are practically coincident up to C_{ext} of 4 × 10⁻² mol and the samples with relatively low C_{ext} plot on this part of the curves. For higher C_{ext} values, samples deviate from the common part of the curves, with an evident shift toward more positive δ¹³C_{ext} values caused by CO₂ degassing and calcite precipitation.

Samples explained by Model 2 are likely groundwaters that transport CO₂ in solution and released it when they emerge at surface (P = 1 bar). Samples plotting between Model 2 and Model 3 can instead be explained by solutions that experienced degassing at 1 < pCO₂ < 10 bar.

In Fig. 8, the range of variation of the carbon isotopic composition (δ¹³C) of calcite (pink dashed bands) and of CO₂ (green dashed bands) predicted by theoretical models are compared to the δ¹³C of (i) TDIC of water samples, (ii) calcite samples from Cézallier and Sainte-Marguerite (Casanova et al., 1999), and (iii) free gas escaping from bubbling springs and mofetes at Monts Dore, Chaîne des Puys, Sainte-Marguerite, Cézallier (Bräuer et al., 2017) and Châteauneuf-les-Bains (Fouillac et al., 1976).

The theoretical ranges of δ¹³C have been computed by applying the

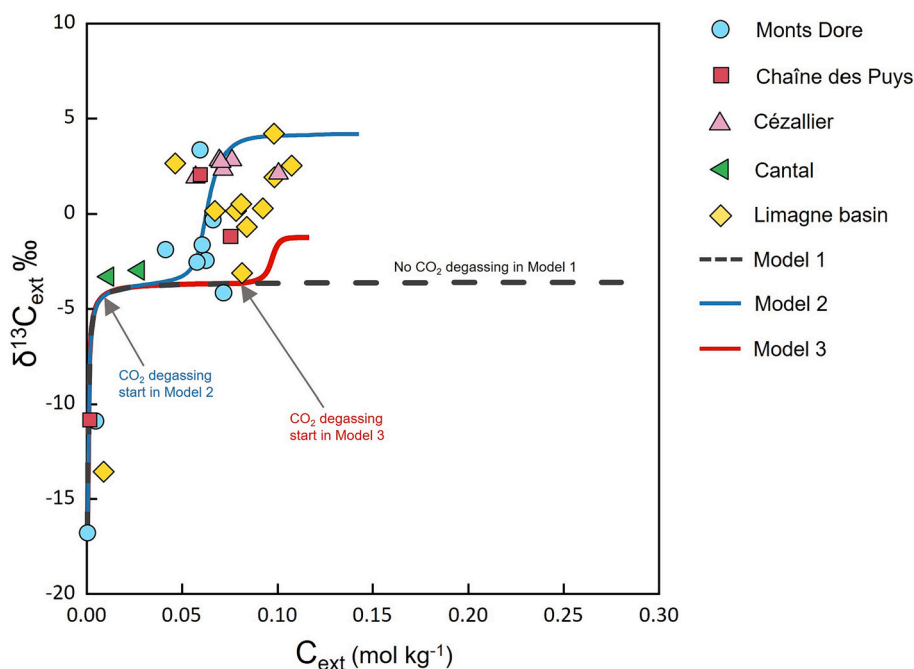


Fig. 7. $\delta^{13}\text{C}_{\text{ext}}$ vs. C_{ext} diagram of the analyzed springs. The theoretical evolution of groundwaters as computed by Model 1, Model 2 and Model 3 is also shown (see text).

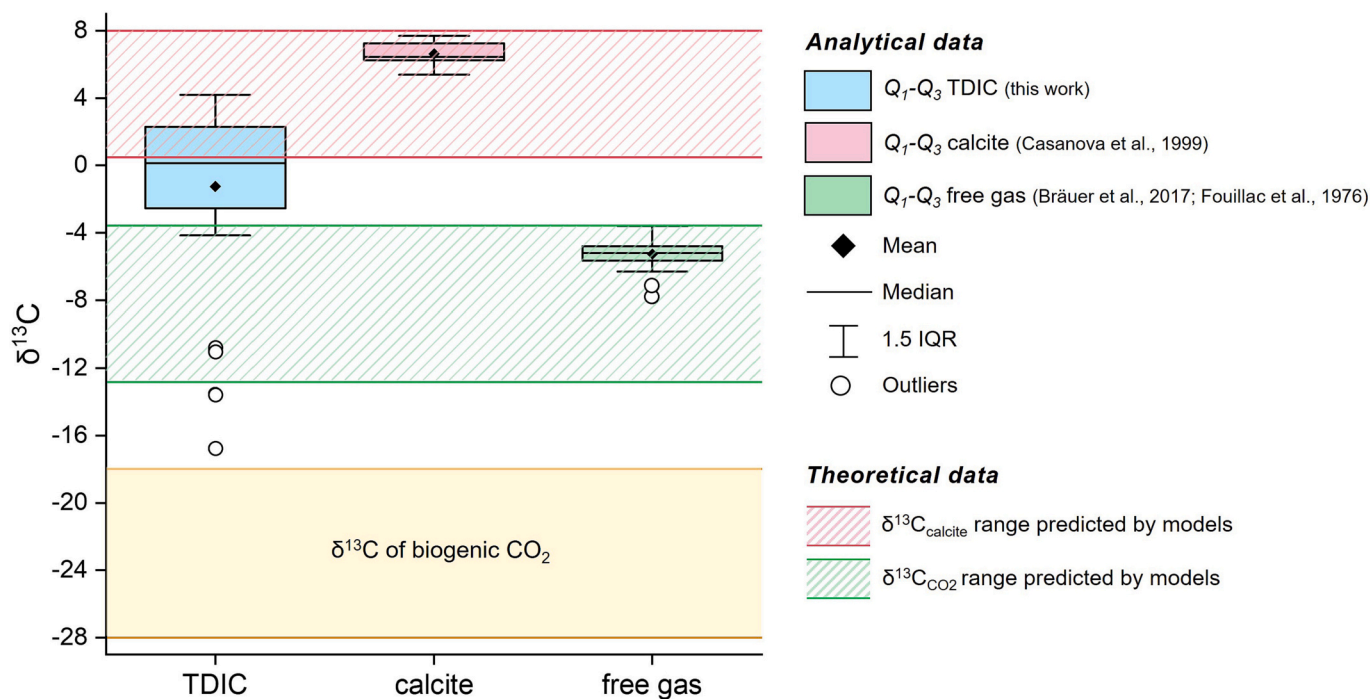


Fig. 8. Comparison between analytical and theoretical $\delta^{13}\text{C}$ values. Box plots show the analytical $\delta^{13}\text{C}$ values of TDIC of groundwaters (light blue box plot, this work), calcite (pink box plot, Casanova et al., 1999) and free gas phases (green box plot, Bräuer et al., 2017; Fouillac et al., 1976). The pink and green dashed bands are respectively the $\delta^{13}\text{C}$ ranges of precipitated calcite and of degassed CO_2 predicted by theoretical models explained in the text. Figure also shows the range of biogenic CO_2 (yellow band, after Chiodini et al., 2000). (For interpretation of the references to colour in this figure legend, the reader is referred to the web version of this article.)

fractionation factors by Clark and Fritz (1997). The comparison between theoretical and analytical values shows that the isotopic composition of free gas samples ($-7.82 < \delta^{13}\text{C}_{\text{CO}_2} < -3.8\text{‰}$, Bräuer et al., 2017; Fouillac et al., 1976) and of calcite samples ($+6.1 < \delta^{13}\text{C}_{\text{calcite}} < +7.7\text{‰}$, Casanova et al., 1999) fall, respectively, in the theoretical fields of CO_2 and calcite predicted by models. The $\delta^{13}\text{C}_{\text{TDIC}}$ of samples ranges from

-16.78‰ to $+4.2\text{‰}$ and plots between (and partly overlap) the isotopic composition of calcite and CO_2 computed by the models. This simple observation suggests that the relatively light $\delta^{13}\text{C}$ of free gas and the relatively heavy $\delta^{13}\text{C}$ of calcite likely derive from the fractionation processes occurring during CO_2 degassing and calcite precipitation starting from the TDIC of the solution. Only four samples show very low

$\delta^{13}\text{C}$ of TDIC (from -16.78‰ to -10.84‰). These samples, that statistically are interpreted as outliers in Fig. 8, have been collected from low salinity springs not involved in the degassing process.

4.6. Computation of the deep carbon emission rate

In order to reconstruct the original carbon content at aquifer conditions, the TDIC of the samples that, at sampling conditions, are oversaturated with calcite ($\text{SI}_{\text{calcite}} > 0$) have been re-computed with the PHREEQC version 3 code (Parkhurst and Appelo, 2013) increasing the pCO_2 until the equilibrium with calcite was achieved. The obtained values (TDIC_c) represent the total carbon content at aquifer conditions immediately before the beginning of the gas-liquid separation process. This correction has been done considering the temperatures at spring emergence and not the temperatures computed through the Na–Li geothermometer because it is unknown at which depth (and, consequently, at which temperature) the gas-water separation starts. Therefore, the TDIC values must be considered as minimum estimations. For the samples that at the surface are in equilibrium or undersaturated with respect to calcite ($\text{SI}_{\text{calcite}} \leq 0$) $\text{TDIC} = \text{TDIC}_c$.

For each sample, the amount of deeply derived carbon ($C_{\text{deep},c}$) has been computed using the following equation:

$$C_{\text{deep},c} = C_{\text{ext},c} - C_{\text{inf}} \quad (7)$$

where C_{inf} is the carbon content of infiltrating waters (here considered as $4.91 \times 10^{-4} \text{ mol kg}^{-1}$) and $C_{\text{ext},c}$ is computed from the TDIC_c by subtracting the C_{carb} .

The emission rate of deeply derived CO_2 (rC_{deep}) associated to each spring/well is given by:

$$rC_{\text{deep}} = C_{\text{deep},c} \times Q \quad (8)$$

where Q is the water flow rate of each spring/well (listed in Supplementary material 1). The computed TDIC, TDIC_c , $C_{\text{ext},c}$, C_{carb} , $C_{\text{deep},c}$ and the rC_{deep} are reported in Supplementary material 3.

The TDIC values range between 0 and $1.64 \times 10^{-1} \text{ mol kg}^{-1}$, while the computed TDIC_c ranges from 0 to $3.20 \times 10^{-1} \text{ mol kg}^{-1}$. Both TDIC and TDIC_c values (Fig. 9a,b) show a bimodal distribution, with a low TDIC population comprising about 26% of samples and an high TDIC population, including the remaining 74% of samples. In the low TDIC population, TDIC and TDIC_c values are practically the same: TDIC ranges from 0 to $3.07 \times 10^{-2} \text{ mol kg}^{-1}$ (median = $1.66 \times 10^{-3} \text{ mol kg}^{-1}$); TDIC_c between 0 and $3.70 \times 10^{-2} \text{ mol kg}^{-1}$ (median = $1.67 \times 10^{-3} \text{ mol kg}^{-1}$). The high TDIC population is characterized by TDIC from $4.14 \times 10^{-2} \text{ mol kg}^{-1}$ to $1.64 \times 10^{-1} \text{ mol kg}^{-1}$ (median = $7.47 \times 10^{-2} \text{ mol kg}^{-1}$) and TDIC_c from $4.14 \times 10^{-2} \text{ mol kg}^{-1}$ to $3.20 \times 10^{-1} \text{ mol kg}^{-1}$ (median = 0.10 mol kg^{-1}), indicating that these waters are oversaturated with respect to calcite and CO_2 . The computed $C_{\text{deep},c}$ ranges from 0 to $3.19 \times 10^{-1} \text{ mol kg}^{-1}$, with the low TDIC group characterized by $0 < C_{\text{deep},c} < 3.65 \times 10^{-2} \text{ mol kg}^{-1}$ (median = $1.17 \times 10^{-3} \text{ mol kg}^{-1}$) and the high TDIC group characterized by $4.09 \times 10^{-2} < C_{\text{deep},c} < 3.19 \times 10^{-1} \text{ mol kg}^{-1}$ (median = $1.01 \times 10^{-1} \text{ mol kg}^{-1}$).

The distribution of the flow rates is positively skewed (skewness = 6.7, mean = 3.98 l s^{-1} , median = 0.67 L s^{-1} , mode = 0.10 L s^{-1}) and shows a log-normal distribution (Fig. 9d), with about 10% of springs with $Q > 10 \text{ L s}^{-1}$ and the remaining characterized by Q of a few L s^{-1} or lower. Flow rates higher than 10 L s^{-1} only occur in volcanic areas (Monts Dore, Cantal and Chaîne des Puys) and are associated with low $C_{\text{deep},c}$ contents ($C_{\text{deep},c} < 1.2 \times 10^{-3} \text{ mol kg}^{-1}$). The only exception is Montpensier spring (sample 163), located along the Aigueperse fault, which has a flow rate of 16.67 L s^{-1} and a $C_{\text{deep},c}$ content of $1.3 \times 10^{-1} \text{ mol kg}^{-1}$. The repartition of flow rates between the different areas is shown in Fig. 9e.

The rC_{deep} values, computed for each spring, range from 0 to $6.83 \times 10^7 \text{ mol yr}^{-1}$ and the computed emission rate, given by the sum of all the individual rC_{deep} values, is $4.5 \pm 0.5 \times 10^8 \text{ mol yr}^{-1}$ (Table 3). Analysing the geographic distribution of the emission rate it is noteworthy that about 68% of the total emission ($3.0 \pm 0.3 \times 10^8 \text{ mol yr}^{-1}$) is from the Limagne Basin, where the 39 Vichy springs alone provide $1.8 \pm 0.2 \times$

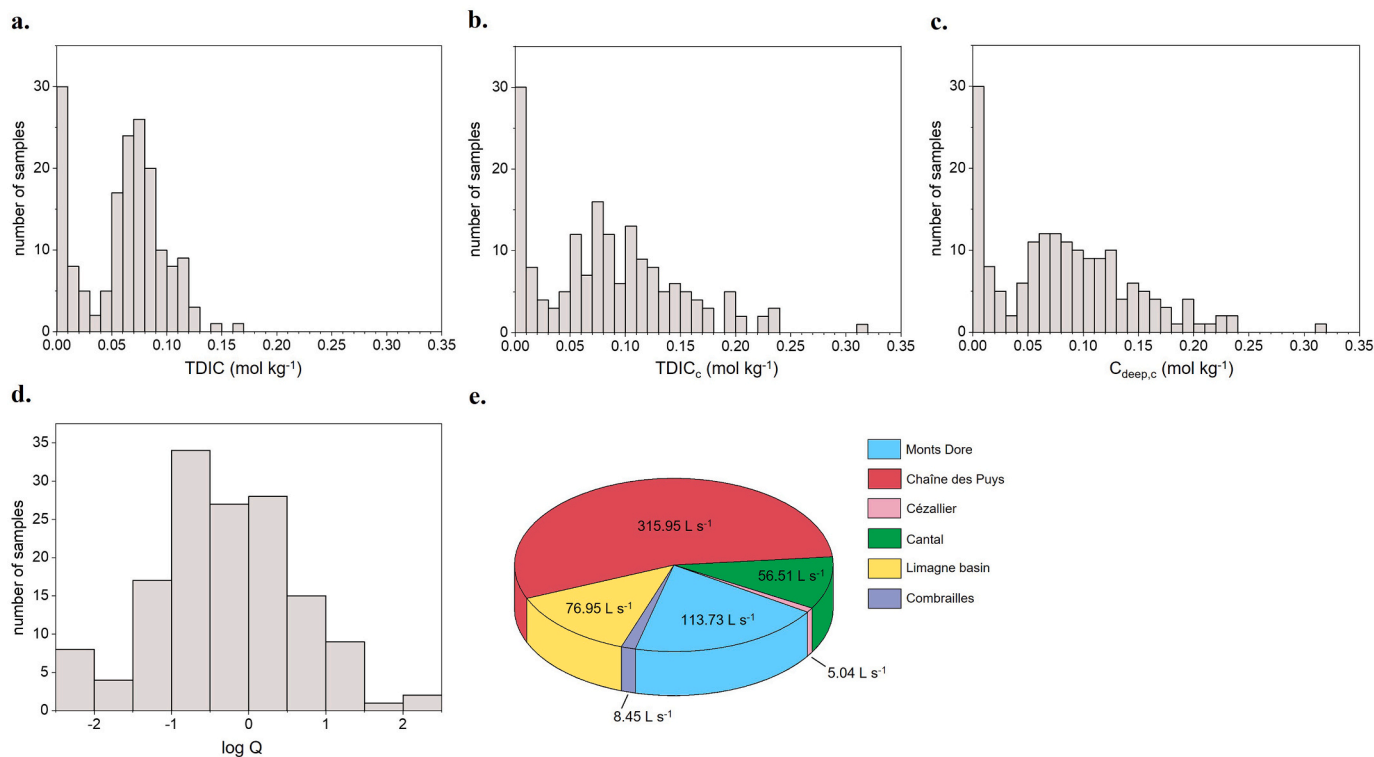


Fig. 9. Frequency distribution of: a. the TDIC b. the TDIC_c c. the $C_{\text{deep},c}$ d. the flow rates (expressed as logarithmic values) e. Repartition of the flow rates between the studied areas.

Table 3

Deeply derived carbon fluxes of the French Massif Central. Column 1 consider measured data, column 2 consider data extrapolated for the Vichy basin and the contribution of Escarot and Lac Pavin.

Area	rC _{deep} (mol yr ⁻¹)	extrapolated rC _{deep} (mol yr ⁻¹)
Monts Dore	$6.0 \pm 0.7 \times 10^7$	$6.0 \pm 0.7 \times 10^7$
Chaîne des Puys	$3.8 \pm 0.4 \times 10^7$	$3.8 \pm 0.4 \times 10^7$
Combrailles	$2.7 \pm 0.3 \times 10^7$	$2.7 \pm 0.3 \times 10^7$
Cézallier	$1.3 \pm 0.1 \times 10^7$	$1.3 \pm 0.1 \times 10^7$
Cantal	$6.8 \pm 0.7 \times 10^6$	$6.8 \pm 0.7 \times 10^6$
Limagne Basin	$3.0 \pm 0.2 \times 10^8$	$1.2 \pm 0.1 \times 10^9$
Escarot		$1.8 \pm 0.4 \times 10^8$
Lac Pavin		$1.7 \pm 0.6 \times 10^6$
Total	$4.5 \pm 0.5 \times 10^8$	$1.52 \pm 0.14 \times 10^9$

10^8 mol yr⁻¹. The volcanic areas of the Monts Dore ($6.0 \pm 0.7 \times 10^7$ mol yr⁻¹), Chaîne des Puys ($3.8 \pm 0.4 \times 10^7$ mol yr⁻¹) and Cézallier ($1.3 \pm 0.1 \times 10^7$ mol yr⁻¹), as well as the Combrailles area ($2.7 \pm 0.3 \times 10^7$ mol yr⁻¹), where the metamorphic basement outcrops, are characterized by an emission rate one order of magnitude lower than the Limagne Basin. Finally, the Cantal volcano shows the lowest emission rate ($6.8 \pm 0.7 \times 10^6$ mol yr⁻¹), which is two order of magnitude lower than the Limagne basin.

The computed flux is a minimum estimate of the degassing process that affects the French Massif Central because i) some small springs have not been sampled, ii) the flow rate data of some springs from literature are not available, making impossible to estimate rC_{deep} for them and iii) the deep carbon released from diffuse soil emissions and volcanic lakes has not been considered.

The CO₂ emission rate from Lac Pavin ($1.7 \pm 0.6 \times 10^6$ mol yr⁻¹, Aeschbach-Hertig et al., 1999) and from the Escarot gas seep ($1.8 \pm 0.4 \times 10^8$ mol yr⁻¹, Gal et al., 2018) suggest that the CO₂ released from the numerous volcanic lakes of the study area and from diffuse soil degassing could play a role in the degassing process, supplying an additional CO₂ amount to the total CO₂ released by the region.

Furthermore, it is worth noting that the Vichy water flow rate used to compute the emission rate (46.58 L s^{-1}) is just a part of the total Vichy flow rate (266.18 L s^{-1} , Bertin and Rouzaire, 2004) thus the emission rate from Vichy is strongly underestimated. In fact, considering the total authorized flow rate from the Vichy basin and the average C_{deep,c} of Vichy springs (1.28×10^{-1} mol kg⁻¹), we can extrapolate a total emission rate from the Vichy basin of $1.1 \pm 0.1 \times 10^9$ mol yr⁻¹ bringing the emission rate of the Limagne basin to $1.2 \pm 0.1 \times 10^9$ mol yr⁻¹.

Considering i) the Vichy extrapolation; ii) the Lac Pavin contribution (Aeschbach-Hertig et al., 1999) and iii) the Escarot contribution (Gal et al., 2018), the total emission rate from the French Massif Central is $1.52 \pm 0.14 \times 10^9$ mol yr⁻¹ (Table 3).

Finally, in order to allow the comparison of French Massif Central to other areas, a rough estimation of the C_{deep} flux (fC_{deep}) has been obtained dividing the total emission rate by the surface of the study area (1645 km^2 , uncertainty of 10%). The resulting fC_{deep} amounts to $9.25 \pm 1.94 \times 10^5$ mol yr⁻¹ km⁻².

The measured deeply-derived CO₂ emission rate is $4.5 \pm 0.5 \times 10^8$ mol yr⁻¹ and the total emission rate extrapolated considering the correction for Vichy and the contribution of Escarot and Lac Pavin amounts to $1.52 \pm 0.14 \times 10^9$ mol yr⁻¹, with a CO₂ flux of $9.25 \pm 1.94 \times 10^5$ mol yr⁻¹ km⁻². Most of the total emission rate is released by the Limagne Basin, suggesting that the large scale normal faults of the Limagne semi-graben structure drive fluid circulation and represent the main path through which the deep gas rises toward the surface.

The French Massif Central CO₂ emission rate is of the same order of magnitude or lower than medium to high enthalpy geothermal systems worldwide (e.g. Salton Trough geothermal system, $\sim 10^9$ mol yr⁻¹, Kerrick et al., 1995; Taupo Volcanic Zone, $\sim 8 \times 10^9$ mol yr⁻¹, Kerrick et al., 1995; Mount Amiata, 2.1×10^9 mol yr⁻¹, Frondini et al., 2009).

The comparison of our data to the estimations done for active rifts

highlights that our estimates are one order of magnitude lower than the mantle-derived CO₂ flux measured at the Magadi-Natron basin (9×10^{10} mol yr⁻¹, Lee et al., 2016) and the total CO₂ emission from the central and northern Mean Ethiopian rift ($1.2\text{--}9.9 \times 10^{10}$ mol yr⁻¹, Hunt et al., 2017), but are of the same order of magnitude of Olkaria Volcanic Complex (2.35×10^9 mol yr⁻¹, Cappelli et al., 2023). This large variability of CO₂ emission rates confirms that more work is needed to quantify the CO₂ flux from continental rifts that, at present, is probably underestimated, as already suggested by Werner et al. (2019) and Foley and Fischer (2017).

5. Conclusions

The present work provides one of the first quantitative estimation of the CO₂ emission released from a passive rift system at regional scale and proposes water-gas-rock interaction models to better constrain the degassing process at the French Massif Central. The water-gas-rock models here proposed are in good agreement with the observed data, highlighting that i) the gas separation from the liquid phase, with bubbles formation and advective rise of the gas toward the surface occurs in a P-T range between 10 bar-180 °C and 1 bar-10 °C; ii) the isotopic composition of the inorganic carbon dissolved in waters, the free gas phase and the precipitated calcite is mainly due to the fractionation processes occurring during CO₂ degassing and calcite precipitation.

The deeply-derived CO₂ emission rate at French Massif Central is $1.52 \pm 0.14 \times 10^9$ mol yr⁻¹, corresponding to a CO₂ flux of $9.25 \pm 1.94 \times 10^5$ mol yr⁻¹ km⁻². The CO₂ emission rate is of the same order of magnitude than the mantle-derived CO₂ emission rate from the Magadi-Natron basin hydrothermal system (Eastern EAR, 5.31×10^9 mol yr⁻¹, Lee et al., 2017).

If compared to other extensional areas, the French Massif Central deeply-sourced CO₂ emission rate is about one order of magnitude lower than the CO₂ emission rate from back-arc basins (i.e. Taupo Volcanic Zone, $8\text{--}10 \times 10^9$ mol yr⁻¹, Kerrick et al., 1995; Seward and Kerrick, 1996) and two order of magnitude lower than the CO₂ emission rate from the Tuscan Roman degassing structure (1.4×10^{11} mol yr⁻¹, Chiodini et al., 2004) and the Campanian degassing structure (0.7×10^{11} mol yr⁻¹, Chiodini et al., 2004) of central-southern Italy.

Finally, it is noteworthy that the total emission rate from the French Massif Central is one order of magnitude higher than the regional emission rate from Eger rift, the eastern sector of ECRIS (3.6×10^8 mol yr⁻¹, Weinlich et al., 1999). This indicates a variability in the magnitude of the CO₂ degassing within the ECRIS system, to which both the French Massif Central and the Eger rift belong, and suggests that more detailed studies are required in other regions of the ECRIS system (e.g. East and West Eifel, Rhine graben, Bohemian Massif) in order to quantify its contribution to the global carbon budget.

CRedit authorship contribution statement

Lisa Ricci: Writing – original draft, Visualization, Software, Methodology, Investigation, Formal analysis, Data curation, Conceptualization. **Francesco Frondini:** Writing – original draft, Visualization, Supervision, Software, Methodology, Investigation, Funding acquisition, Data curation, Conceptualization. **Daniele Morgavi:** Writing – original draft, Visualization, Investigation. **Marino Vetusch Zuccolini:** Writing – original draft, Visualization, Software, Methodology. **Guillaume Boudoire:** Writing – original draft, Visualization, Investigation. **Mickael Laumonier:** Writing – original draft, Visualization, Investigation. **Stefano Caliro:** Writing – original draft, Methodology, Investigation, Formal analysis. **Carlo Cardellini:** Writing – original draft, Visualization. **Artur Ionescu:** Writing – original draft, Visualization. **Alessandra Ariano:** Writing – original draft. **Giovanni Chiodini:** Writing – original draft, Visualization, Supervision, Methodology, Conceptualization.

Declaration of competing interest

The authors declare that they have no known competing financial interests or personal relationships that could have appeared to influence the work reported in this paper.

Data availability

The authors declare that the data supporting the findings of this study are available within the supplementary information files.

Acknowledgements

This work was supported by PRIN PROJECT 2017 Connect4Carbon.

Appendix A. Supplementary data

Supplementary data to this article can be found online at <https://doi.org/10.1016/j.chemgeo.2024.122012>.

References

- Aeschbach-Hertig, W., Hofer, M., Kipfer, R., Imboden, D.M., Wieler, R., 1999. Accumulation of mantle gases in a permanently stratified volcanic lake (Lac Pavin, France). *Geochim. Cosmochim. Acta* 63, 3357–3372.
- Aumar, C., 2022. Modélisation de la topographie antévolcanique de la chaîne des Puys. Implications hydrogéologiques pour les bassins versants de la Veyre et de Côme. Thèse d'Université. Clermont-Ferrand, 313 pp.
- Battani, A., Deville, E., Faure, J.L., Noirez, S., Tocqué, E., Benoît, Y., Schmitz, J., Parlouar, D., Sarda, P., Gal, F., Le Pierres, K., Brach, M., Braibant, G., Beny, C., Pokryszka, Z., Charmoille, A., Bentivegna, G., Pironon, J., de Donato, P., Garnier, C., Cailteau, C., Barrès, O., Radilla, G., Bauer, A., 2010. Geochemical Study of Natural CO₂ Emissions in the French Massif Central: how to Predict Origin, Processes and Evolution of CO₂ Leakage. *Oil Gas Sci. Technol. Rev. d'IFP Energ. Nouvelles Inst. Français Pétrol.* 65 (4), 615–633. <https://doi.org/10.2516/ogst/2009052>.
- Bérard, P., Loizeau, M., Rouzaire, D., Vigouroux, P., 2002a. Amélioration de la connaissance des ressources en eau souterraine des sites thermaux en Auvergne. Site du Mont-Dore (63). Rapport BRGM RP-51941-FR.
- Bérard, P., Loizeau, M., Rouzaire, D., Vigouroux, P., 2002b. Amélioration de la connaissance des ressources en eau souterraine des sites thermaux en Auvergne. Site du Chaudes-Aigues (15). Rapport BRGM RP-51722-FR.
- Bertin, C., Rouzaire, D., 2004. Amélioration de la connaissance des ressources en eau souterraine des sites thermaux en Auvergne – site du bassin de Vichy (03). Rapport BRGM RP-53095-FR.
- Bertin, C., Rouzaire, D., Vigouroux, P., 2003. Amélioration de la connaissance des ressources en eau souterraine des sites thermaux en Auvergne site de Châteauneuf-les-Bains (63). Rapport BRGM RP-52471-FR.
- Bodiseltisch, B., Montanari, A., Koeberl, C., Coccioni, R., 2004. Delayed climate cooling in the late Eocene caused by multiple impacts: high-resolution geochemical studies at Massignano, Italy. *Earth Planet. Sci. Lett.* 223, 283–302.
- Boudoire, G., Pasdeloup, G., Schiavi, F., Cluzel, N., Raffin, V., Grassa, F., Giuffrida, G., Liuzzo, M., Harris, A., Laporte, D., Rizzo, A.L., 2023. Magma storage and degassing beneath the youngest volcanoes of the Massif Central (France): Lessons for the monitoring of a dormant volcanic province. *Chem. Geol.* 634 <https://doi.org/10.1016/j.chemgeo.2023.121603>.
- Bräuer, K., Kämpf, H., Niedermann, S., Wetzel, H.-U., 2017. Regional distribution pattern of carbon and helium isotopes from different volcanic fields in the French Massif Central: evidence for active mantle degassing and water transport. *Chem. Geol.* 469, 4–18.
- Brune, S., Corti, G., Ranalli, G., 2017. Controls of inherited lithospheric heterogeneity on rift linkage: Numerical and analog models of interaction between the Kenyan and Ethiopian rifts across the Turkana depression. *Tectonics* 36 (9), 1767–1786. <https://doi.org/10.1002/2017TC004739>.
- Brune, S., Kolawole, F., Olive, J.-A., Stamps, D.S., Buck, W.R., Buiter, S.J.H., Furman, T., Shillington, D.J., 2023. Geodynamics of continental rift initiation and evolution. *Nat. Rev. Earth Environ.* 4, 235–253. <https://doi.org/10.1038/s43017-023-00391-3>.
- Caliro, S., Chiodini, G., Avino, R., Cardellini, C., Frondini, F., 2005. Volcanic degassing at Somma-Vesuvio (Italy) inferred by chemical and isotopic signatures of groundwaters. *Appl. Geochem.* 20, 1060–1076. <https://doi.org/10.1016/j.apgeochem.2005.02.002>.
- Cappelli, L., Wallace, P.A., Randazzo, A., Kamau, P.M., Njoroge, R.W., Otieno, V., Tubula, M.S., Mariita, N.O., Mangi, P., Fontijn, K., 2023. Diffuse soil CO₂ emissions at rift volcanoes: Structural controls and total budget of the Olkaria Volcanic complex (Kenya) case study. *J. Volcanol. Geotherm. Res.* 443, 107929 <https://doi.org/10.1016/j.jvolgeores.2023.107929>.
- Casanova, J., Bodénan, F., Négrel, P., Azaroual, M., 1999. Microbial control on the precipitation of modern ferrihydrite and carbonate deposits from the Cézallier hydrothermal springs (Massif Central, France). *Sediment. Geol.* 126, 125–145.
- Chiodini, G., 1996. Gases dissolved in groundwaters: analytical methods and examples of applications in central Italy. In: *Proceedings of the Rome Seminar on Environmental Geochemistry*, Castelnuovo di Porto, May 22–26 1996, pp. 135–148.
- Chiodini, G., Frondini, F., Cardellini, C., Parello, F., Peruzzi, L., 2000. Rate of diffuse carbon dioxide Earth degassing estimated from carbon balance of regional aquifers: the case of central Apennine, Italy. *J. Geophys. Res.* 105, 8423–8434.
- Chiodini, G., Cardellini, C., Amato, A., Boschi, E., Caliro, S., Frondini, F., Ventura, G., 2004. Carbon dioxide Earth degassing and seismogenesis in central and southern Italy. *Geophys. Res. Lett.* 31, L07615. <https://doi.org/10.1029/2004GL019480>.
- Clark, I.D., Fritz, P., 1997. *Environmental Isotopes in Hydrogeology*. Lewis Publishers, Boca Raton, FL, p. 328.
- Cornacchia, A., Brandano, M., Raffi, I., Tomassetti, L., Flores, I., 2018. The Eocene–Oligocene transition in the C-isotope record of the carbonate successions in the Central Mediterranean. *Glob. Planet. Chang.* 167, 110–122. <https://doi.org/10.1016/j.gloplacha.2018.05.012>.
- Craig, H., 1961. Isotopic Variations in Meteoric Waters. *Science* 133, 1702–1703.
- D'Amore, F., Panichi, C., 1985. Geochemistry in geothermal exploration. *Int. J. Energy Res.* 9 (3), 277–298. <https://doi.org/10.1002/er.4440090307>.
- Delany, J.M., Lundeen, S.R., 1990. The LLNL Thermochemical Database. Lawrence Livermore National Laboratory Report UCRL21658, Livermore, CA, 150pp.
- Dèzes, P., Schmid, S.M., Ziegler, P.A., 2004. Evolution of the European Cenozoic Rift System: interaction of the Alpine and Pyrenean orogens with their foreland lithosphere. *Tectonophysics* 389, 1–33.
- Downes, H., Reichow, M.K., Mason, P.R.D., Beard, A.D., Thirlwall, M.F., 2003. Mantle domains in the lithosphere beneath the French Massif Central: trace element and isotopic evidence from mantle clinopyroxenes. *Chem. Geol.* 200 (1–2), 71–87. [https://doi.org/10.1016/S0009-2541\(03\)00126-8](https://doi.org/10.1016/S0009-2541(03)00126-8).
- Foley, F.S., Fischer, T.P., 2017. An essential role for continental rifts and lithosphere in the deep carbon cycle. *Nat. Geosci.* 10, 897–902. <https://doi.org/10.1038/s41561-017-0002-7>.
- Fouillac, C., 1983. Chemical geothermometry in CO₂-rich thermal waters. Example of the French Massif Central. *Geothermics* 12 (2–3), 149–160. [https://doi.org/10.1016/0375-6505\(83\)90025-1](https://doi.org/10.1016/0375-6505(83)90025-1).
- Fouillac, C., Michard, G., Merlivat, L., Javoy, M., Jouzel, J., 1976. Etude géochimique des eaux thermominérales de Châteauneuf-les-Bains. *J. Français Hydrol.* 7, 151–157.
- Fouillac, C., Fouillac, A.M., Chery, L., 1991. Isotopic studies of deep and surface waters in the French Massif Central. In: *Proc. Int. Symp. Isotope Techniques in Water Resources Development*, 11–15 March 1991, Vienna, pp. 646–648.
- Fournier, R.O., 1979. A revised equation for the Na/K geothermometer. *Geotherm. Res. Council* 3, 221–224.
- Frondini, F., Caliro, S., Cardellini, C., Chiodini, G., Morgantini, N., 2009. Carbon dioxide degassing and thermal energy release in the Monte Amiata volcanic-geothermal area (Italy). *Appl. Geochem.* 24 (9), 860–875. <https://doi.org/10.1016/j.apgeochem.2009.01.010>.
- Frondini, F., Cardellini, C., Caliro, S., Beddini, G., Rosiello, A., Chiodini, G., 2019. Measuring and interpreting CO₂ fluxes at regional scale: the case of the Apennines, Italy. *J. Geol. Soc.* 176, 408–416. <https://doi.org/10.1144/jgs2017-169>.
- Gal, F., Leconte, S., Gadalia, A., 2018. The “Escarot” gas seep, French Massif Central: CO₂ discharge from a quiescent volcanic system- Characterization and quantification of the gas emissions. *J. Volcanol. Geotherm. Res.* 353, 68–82.
- Gibson, J.J., Birks, S.J., Edwards, T.W.D., 2008. Global prediction of δA and δ2H-618O evaporation slopes for lakes and soil water accounting for seasonality. *Glob. Biogeochem. Cycles* 22 (2). <https://doi.org/10.1029/2007GB002997>.
- Giggenbach, W.F., 1988. Geothermal solute equilibria. Derivation of Na-K-Mg-Na geothermometers. *Geochim. Cosmochim. Acta* 52, 2749–2765.
- Giggenbach, W.F., Goguel, R.L., 1989. Collection and Analysis of Geothermal and Volcanic Water and Gas Discharges. Report No. CD 2401. Chemistry Division, DSIR, Petone, New Zealand.
- Hermanson, P.H., Akerblom, G., Chyssler, J., Linden, A., 1991. Geogas—A Carrier or a Tracer? Statens Karnbransle Namnd (SKN) Report 51. National Board for Spent Nuclear Fuel, Stockholm, p. 66.
- Hunt, J.A., Zafu, A., Mather, T.A., Pyle, D.M., Barry, P.H., 2017. Spatially Variable CO₂ Degassing in the Main Ethiopian Rift: Implications for Magma Storage, Volatile Transport, and Rift-Related Emissions. *Geochem. Geophys. Geosyst.* 18 (10), 3714–3737. <https://doi.org/10.1002/2017GC006975>.
- Karolytė, R., Serno, S., Johnson, G., Gilfillan, S.M.V., 2017. The influence of oxygen isotope exchange between CO₂ and H₂O in natural CO₂-rich spring waters: Implications for geothermometry. *Appl. Geochem.* 84, 173–186.
- Kern, Z., Hatvani, I.G., Czuppon, G., Fórizs, I., Erdélyi, D., Kanduć, T., Palcsu, L., Vreča, P., 2020. Isotopic ‘Altitude’ and ‘Continental’ Effects in Modern Precipitation across the Adriatic-Pannonian Region. *Water* 12 (6), 1797. <https://doi.org/10.3390/w12061797>.
- Kerrick, D.M., 2001. Present and past non-anthropogenic CO₂ degassing from the solid earth. *Rev. Geophys.* 39 (4), 565–585.
- Kerrick, D.M., McKibben, M.A., Seward, T.M., Caldeira, K., 1995. Convective hydrothermal CO₂ emission from high heat flow regions. *Chem. Geol.* 121 (1–4), 285–293. [https://doi.org/10.1016/0009-2541\(94\)00148-2](https://doi.org/10.1016/0009-2541(94)00148-2).
- Ladouce, B., Luc, A., Nathalie, D., 2009. Chemical and isotopic investigation of rainwater on Southern France (1996–2002): potential use as input signal for karst functioning investigation. *J. Hydrol.* 367, 150–164.
- Lee, H., Fischer, T.P., Muirhead, J.D., Ebinger, C.J., Kattenhorn, S.A., Sharp, Z.D., Kianji, G., Takahata, N., Sano, Y., 2017. Incipient rifting accompanied by the release of subcontinental lithospheric mantle volatiles in the Magadi and Natron basin, East Africa. *J. Volcanol. Geotherm. Res.* 346, 118–133. <https://doi.org/10.1016/j.jvolgeores.2017.03.017>.

- Lee, H., Muirhead, J.D., Fischer, T.P., Ebinger, C.J., Kattenhorn, S.A., Sharp, Z.D., Kianji, G., 2016. Massive and prolonged deep carbon emissions associated with continental rifting. *Nat. Geosci.* 9, 145–149. <https://doi.org/10.1038/ngeo2622>.
- Lehnert, K., Su, Y., Langmuir, C.H., Sarbas, B., Nohl, U., 2000. A global geochemical database structure for rocks. *Geochem. Geophys. Geosyst.* 1, 1012. <https://doi.org/10.1029/1999GC000026>.
- Maréchal, J.-C., Rouillard, J., 2020. Groundwater in France: Resources, use and Management Issues. In: Rinaudo, J.D., Holley, C., Barnett, S., Montginoul, M. (Eds.), *Sustainable Groundwater Management. Global Issues in Water Policy*, vol. 24. Springer, Cham, pp. 17–45. https://doi.org/10.1007/978-3-030-32766-8_2.
- Matthews, A., Fouillac, C., Hill, R., O'Nions, R.K., Oxburgh, E.R., 1987. Mantle-derived volatiles in continental crust: the Massif Central of France. *Earth Planet. Sci. Lett.* 85, 117–128.
- Maury, C., Brousse, R., Villemant, B., Joron, J.-L., Jaffrezic, H., Treuil, M., 1980. Cristallisation fractionnée d'un magma basaltique alcalin: la série de la Chaîne des Puys (Massif central, France). I. Pétrologie. *Bull. Mineral.* 103-2, 250–266.
- Merle, O., Aumar, C., Labazuy, P., Merciecca, C., Buvat, S., 2023. Structuration tertiaire et quaternaire du Plateau des Dômes (Chaîne des Puys, Massif central, France). *Géol. Fr.* 1, 1–22.
- Michard, G., 1990. Behaviour of major elements and some trace elements (Li, Rb, Cs, Sr, Fe, Mn, W, F) in deep hot waters from granitic areas. *Chem. Geol.* 89, 117–134. [https://doi.org/10.1016/0009-2541\(90\)90062-C](https://doi.org/10.1016/0009-2541(90)90062-C).
- Michard, G., Stettler, A., Fouillac, C., Ouzounian, G., Mandeville, D., 1976. Subsuperficial changes in chemical composition of the thermomineral waters of Vichy basin, geothermal implications. *Geochem. J.* 10, 155–161.
- Michon, L., Merle, O., 2001. The evolution of the Massif Central rift: spatio-temporal distribution of the volcanism. *Bull. Soc. Géol. France* 172 (2), 201–211.
- Millot, R., Négrel, P., Petelet-Giraud, E., 2007. Multi-isotopic (Li, B, Sr, Nd) approach for geothermal reservoir characterization in the Limagne Basin (Massif Central, France). *Appl. Geochem.* 22, 2307–2325.
- Millot, R., Petelet-Giraud, E., Guerrot, C., Négrel, P., 2010. Multi-isotopic composition ($\delta^7\text{Li}$ - $\delta^{11}\text{B}$ - δ^{D} - $\delta^{18}\text{O}$) of rainwaters in France: Origin and spatio-temporal characterization. *Appl. Geochem.* 25, 1510–1524.
- Négrel, P., Roy, S., 1998. Chemistry of the rainwater in the Massif Central (France): a strontium isotope and major element study. *Appl. Geochem.* 13 (8), 941–952. [https://doi.org/10.1016/S0883-2927\(98\)00029-8](https://doi.org/10.1016/S0883-2927(98)00029-8).
- Négrel, P., Guerrot, C., Cocherie, A., Azaroual, M., Brach, M., Fouillac, C., 2000. Rare earth elements, neodymium and strontium isotopic systematics in mineral waters: evidence from the Massif Central, France. *Appl. Geochem.* 15, 1345–1367.
- Nehlig, P., Boivin, P., De Goër, A., Mergoïl, J., Proureau, G., Sustrac, G., Thiéblemont, D., 2003. Les volcans du Massif Central. *Revue Géologues, Numéro spécial Massif central*.
- Nomade, S., Pastre, J.-F., Nehlig, P., Guillou, H., Scao, V., Scaillet, S., 2014. Tephrochronology of the Mont Dore volcanic Massif (Massif Central, France): new $^{40}\text{Ar}/^{39}\text{Ar}$ constraints on the late Pliocene and early Pleistocene activity. *Bull. Volcanol.* 76, 798. <https://doi.org/10.1007/s00445-014-0798-6>.
- Parkhurst, D.L., Appelo, C.A.J., 2013. Description of input and examples for PHREEQC version 3: a computer program for speciation, batch-reaction, one-dimensional transport, and inverse geochemical calculations. U.S. Geological Survey Techniques and Methods. <https://doi.org/10.3133/tm6A43> book 6, chap. A43, 497 p.
- Pauwels, H., Fouillac, C., Goff, F., Vuataz, F.-D., 1997. The isotopic composition of CO_2 -rich thermal waters in the Mont-Dore region (Massif-Central, France). *Appl. Geochem.* 12, 411–427.
- Pfahl, S., Soderemann, H., 2014. What controls deuterium excess in global precipitation? *Clim. Past Discuss.* 9 (4), 4745–4770. <https://doi.org/10.5194/cpd-9-4745-2013>.
- Poage, M.A., Chamberlain, C.P., 2001. Empirical Relationships between Elevation and the Stable Isotope Composition of Precipitation and Surface Waters: Considerations for Studies of Paleoelevation Change. *Am. J. Sci.* 301, 1–15. <https://doi.org/10.2475/ajs.301.1.1>.
- Reubi, O., Hernandez, J., 2000. Volcanic debris avalanche deposits of the upper Maronne valley (Cantal Volcano, France): evidence for contrasted formation and transport mechanisms. *J. Volcanol. Geotherm. Res.* 102 (3–4), 271–286.
- Serra, H., Petelet-Giraud, E., Négrel, P., 2003. Inventaire du potentiel géothermique de la Limagne (COPGEN) Synthèse bibliographique de la géochimie des eaux thermales. *Rap. BRGM/RP-52587-FR*.
- Seward, T.M., Kerrick, D.M., 1996. Hydrothermal CO_2 emission from the Taupo Volcanic Zone, New Zealand. *Earth Planet. Sci. Lett.* 139, 105–113.
- Vennin, E., Bouton, A., Roche, A., Gérard, E., Bundeleva, I., Boussagol, P., Wattinne, A., Kolodka, C., Gaucher, E., Virgone, A., Visscher, P.T., 2021. The Limagne Basin: a journey through modern and fossil microbial deposits. *Bull. Soc. Géol. France* 192 (1), 41. <https://doi.org/10.1051/bsgf/2021030>.
- Vuataz, F., Fouillac, A.M., Fouillac, C., Michard, G., Brach, M., 1987. Étude isotopique et suivi géochimique des eaux des sondages de Chassole et de quelques sources minérales du Cézaillier. *Géol. Fr.* 4, 121–131.
- Weinlich, F.H., Bräuer, K., Kämpf, H., Strauch, G., Tesar, J., Weise, S.M., 1999. An active subcontinental mantle volatile system in the western Eger rift, Central Europe: gas flux, isotopic (He, C, and N) and compositional fingerprints. *Geochim. Cosmochim. Acta* 63 (21), 3653–3671. [https://doi.org/10.1016/S0016-7037\(99\)00187-8](https://doi.org/10.1016/S0016-7037(99)00187-8).
- Werner, C., Fischer, T.P., Aiuppa, A., Edmonds, M., Cardellini, C., Carn, S., Chiodini, G., Cottrell, E., Burton, M., Schinohara, H., Allard, P., 2019. Carbon dioxide emissions from subaerial volcanic regions. In: Orcutt, B., Daniel, I., Dasgupta, R. (Eds.), *Deep Carbon: Past to Present*. Cambridge Univ. Press, New York, pp. 188–236.
- Wilson, M., Downes, H., 2006. Tertiary-Quaternary intra-plate magmatism in Europe and its relationship to mantle dynamics. In: Gee, D.G., Stephenson, R. (Eds.), *European Lithosphere Dynamics*, Geological Society of London Memoir 32. Geological Society of London, London, pp. 147–166. ISBN 978-1-86239-212-0.
- Wolery, T.J., 1979. Calculation of Chemical Equilibrium between Aqueous Solution and Minerals- the EQ3/6 Software Package. Lawrence Livermore National Laboratory Report UCRL-52658, Livermore, CA.
- Wolery, T.J., 1992. EQ3/EQ6, a software package for geochemical modelling of aqueous systems, package overview and installation guide (version 7.0). Lawrence Livermore National Laboratory Report UCRL-MA110662(1), Livermore, CA.
- Wolery, T.J., Jarek, R.L., 2003. EQ3/6, Version 8.0—Software User's Manual. Civilian Radioactive Waste Management System, Management & Operating Contractor. Sandia National Laboratories, Albuquerque, New Mexico.